

Regional screening of saline aquifers in the Malay Basin for CO₂ storage

Iain de Jonge-Anderson^{a,b,*}, Hariharan Ramachandran^a, Ana Widyanita^{a,c},
Andreas Busch^d, Florian Doster^a, Uisdean Nicholson^a

^a Institute of GeoEnergy Engineering (IGE), School of Energy, Geoscience, Infrastructure & Society, Heriot-Watt University, Edinburgh, EH14 4AS, UK

^b Department of Civil & Environmental Engineering, University of Strathclyde, Glasgow, G1 1XJ, UK

^c PETRONAS Research Sdn. Bhd., Malaysia

^d Lyell Centre, Heriot-Watt University, Edinburgh, EH14 4AS, UK

ARTICLE INFO

Keywords:

Carbon dioxide storage
CCS
Site screening
Malay Basin
Malaysia
CO₂ storage

ABSTRACT

The Malay Basin has received significant attention for geological carbon dioxide storage (GCS), but there are no published studies addressing the selection of appropriate deep saline aquifers. This study closes this gap. We process spatial data and use geological modelling and cluster analysis to identify optimal areas for GCS, considering various subsurface characteristics such as temperature, pressure, porosity and thermophysical CO₂ properties. It is found that the basin contains numerous Cenozoic aquifers suitable for GCS including locally thick, but low net-to-gross (NTG), stacked formations. Pliocene aquifers are too shallow to offer storage for CO₂ in large quantities, but upper Miocene aquifers located in the northwest of the basin contain promising intervals with significant porosities and conditions favouring denser CO₂. Middle Miocene aquifers, while low NTG, are thick, and optimally located around the margins of the basin. They also have significant storage capacity and could be developed as a stacked GCS site. Lower Miocene aquifers are higher NTG, but deeply buried across many areas of the basin, yet the oldest aquifer evaluated still holds substantial storage capacity, where subject to minor burial at the margins of the basin. Overall, this study provides a novel first assessment of aquifer GCS potential in the Malay Basin, while also contributing to wider efforts to evolve screening workflows for other geological basins.

1. Introduction

Widespread adoption of geological carbon dioxide storage (GCS) is crucial to limiting global warming to 1.5 °C by 2050 (Krevor et al., 2023), necessitating annual storage of up to 30 Gt yr⁻¹ by 2050 (IPCC, 2022). This requires a significant expansion of GCS sites, with current projects only constituting annual storage of 0.009 Gt (Zhang et al., 2024).

Mature sedimentary basins, defined as basins from which hydrocarbons have historically been produced, are prime regions for facilitating GCS because of their favourable geological characteristics and proximity to existing infrastructure. Depleted gas fields in these basins are attractive as they contain large amounts of subsurface data and offer historical evidence of effective storage capacity and retention. However, availability is constrained to those that have ceased production; they are usually closed, confined structures and the depleted reservoir pressures pose distinct engineering challenges (Hughes, 2009). Containment is

predominantly achieved by structural and residual trapping but there is an absence of large scale understanding on stress hysteresis and its impact on rock characteristics, such as fracture pressure (Lynch et al., 2013).

Scaling up GCS will require immediate development of many more storage sites and deep saline aquifers are well-positioned to facilitate this (Gunter et al., 1998). Containment within these sites is achieved by a mixture of structural, residual and solubility trapping, the relative contributions of which will depend on the geometry of the reservoir and migration pathway of the CO₂ plume amongst several other factors. However, less data is typically available for aquifers and hence, uncertainty around reservoir, caprock and fluid properties is larger. Basin screening studies have been undertaken to underpin the optimal regions for GCS (Bachu, 2003; Chadwick et al., 2008; Ramírez et al., 2010; Rodosta et al., 2011; Raza et al., 2016; Bump et al., 2021; Oglund-Hand et al., 2022; Wendt et al., 2022; Proietti et al., 2023; Callas et al., 2024). These studies often rely on either limited data, necessitating broad

* Corresponding author.

E-mail address: iain.de-jonge-anderson@strath.ac.uk (I. de Jonge-Anderson).

<https://doi.org/10.1016/j.ijggc.2025.104347>

Received 6 November 2024; Received in revised form 3 February 2025; Accepted 6 March 2025

Available online 11 March 2025

1750-5836/© 2025 The Author(s). Published by Elsevier Ltd. This is an open access article under the CC BY license (<http://creativecommons.org/licenses/by/4.0/>).

assumptions about the subsurface or very large datasets from hydrocarbon exploration, which results in a more detailed evaluation but at the expense of time and cost. There is a need to evolve GCS screening to overcome the lack of data and provide workflows that are flexible and can be translated to other basins with variable amounts of data associated with them. In this study, a workflow is devised which addresses aspects of this, by utilising previously published data, geological trends and probabilistic techniques.

The Asia-Pacific region will play a prominent role in the global energy transition. Many countries within it are experiencing rapid growth while simultaneously seeking to radically reduce CO₂ emissions, with the region currently accounting for over half of global CO₂ emissions (IEA, 2024). With an area of about 70,000 km² and a sedimentary thickness of up to 13 km (Straume et al., 2019), the Malay Basin is one of the largest geological basins in Southeast Asia. It is also a mature hydrocarbon region, accounting for over 14.8 billion barrels of oil equivalent (Madon, 2021), extracted over many decades. Malaysia is being positioned as a regional Carbon Capture and Storage (CCS) hub (TotalEnergies, 2023) and the Malay Basin has attracted considerable recent interest for GCS (de Jonge-Anderson et al., 2024a,b; PETRONAS, 2024a), however, there is limited scientific literature focused on the geology of the basin, and no studies to date have addressed the issue of selecting appropriate saline aquifers and/or specific areas of the basin for GCS.

We seek to address this by undertaking a regional-scale, geological analysis of the Malay Basin to evaluate the suitability of aquifers for GCS in the basin and highlight the optimal injection regions that can lead to targeted feasibility studies. A series of geological properties key to GCS are addressed, and while this list is not exhaustive, the workflow is framed in such a manner that more properties can be readily added as the screening progresses. The properties incorporated here are pressure, temperature, porosity, fault intensity and CO₂ thermophysical properties and several cut-offs (upper or lower limits) were subsequently applied to these to determine optimal injection zones and providing

indicative estimates of volumetric storage capacity within these zones.

2. Geological setting

The Malay Basin is a Cenozoic extensional basin oriented roughly parallel to the east coast of Peninsular Malaysia (Fig. 1a). The structural history of the basin is well documented following analysis of seismic datasets associated with hydrocarbon production (Tjia and Liew, 1996; Madon and Watts, 1998; Mansor et al., 2014; de Jonge-Anderson et al., 2024b). It initially developed as a series of west-east-oriented rift basins, which formed following Paleogene extension across a broadly NW-SE shear zone. These rift basins were infilled with continental (fluvial, lacustrine) Eocene and Oligocene sediments and most were subsequently inverted during a later phase of deformation in the basin. At the end of the Oligocene (~ 24 Ma), extension ceased, and the basin experienced a phase of post-rift subsidence, leading to more widespread deposition of Miocene shallow marine sediments. During the late Miocene, a regional reorganisation in stresses following the end of seafloor spreading of the South China Sea led to a structural inversion of much of the basin, leading to a shallowing in depositional facies and ultimately a locally deep unconformity during the Tortonian (~ 8 Ma). This uplift event inverted the pre-Miocene syn-rift grabens and deformed much of the overlying stratigraphy into a series of anticlines and ultimately form major hydrocarbon fields. Gentle subsidence renewed during the Pliocene, leading to further shallow marine deposition and limited extensional faulting.

Throughout the basin's history, it remained at or near sea level and there are many recognised sandstone reservoir intervals across the entire stratigraphy from Pliocene-age Group B to Oligocene-age Group N (Fig. 1b) (Madon and Jong, 2021). However, the only published study addressing regional variations in these reservoirs is Madon et al. (1999), with most studies focused on field-specific case studies (e.g. Madon, 1994). Studies of this nature are necessary when considering GCS suitability as the basin lacks a clearly defined, thick target aquifer like those

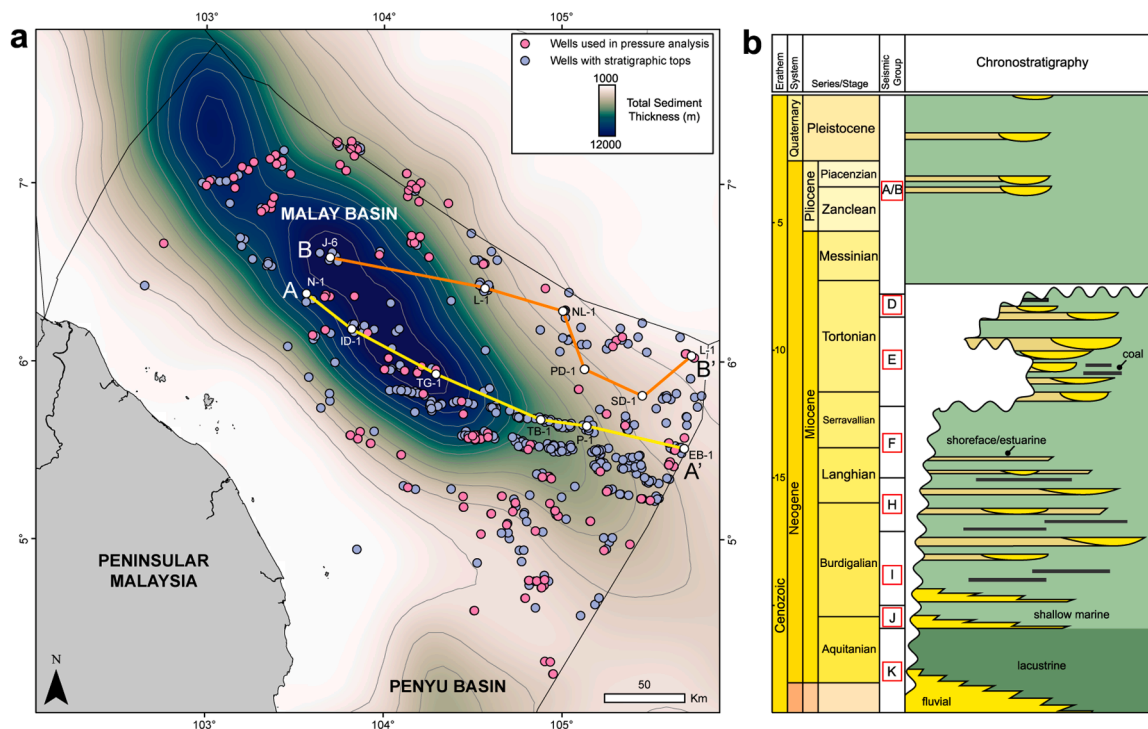


Fig. 1. a). Map of the Malay Basin showing position relative to the east coast of Peninsular Malaysia, the locations of wells with stratigraphic tops available, those with pressure datasets available and locations of the two well correlations presented in Fig. 4. The basemap shows the total sediment thickness at a 100 m contour increment (Straume et al., 2019). b) Simplified chronostratigraphic chart highlighting the aquifers evaluated in this study (after Armitage and Viotti, 1977; Ramli, 1988; Yakzan et al., 1996; Madon et al., 1999; Mansor et al., 2014; Lunt, 2021; de Jonge-Anderson et al., 2024b).

historically selected for early-stage GCS projects such as the UK's Bunter Sandstone Formation (Gibson-Poole et al., 2024) or Norway's Utsira Formation (Chadwick et al., 2004). Over 85 % of reserves are within Miocene sandstones, notably Groups D, E, I, J and K (Fig. 1b) (Madon, 2021) and the best reservoir quality is found in shallow marine sandstones of Groups J and E and braided fluvial sandstones of Group K (Madon et al., 1999). But abrupt changes in sedimentary facies, combined with rapid burial often lead to highly variable reservoir quality, especially at the regional scale, in areas without dense drilling and/or analysis of 3D seismic attributes.

Despite its rich hydrocarbon history, there are currently very few published accounts of the GCS suitability of saline aquifers in the Malay Basin. Previous accounts have highlighted high volumetric storage capacity estimates from 19 to 208 Gt, (Hasbollah et al., 2020; Zhang and Lau, 2022), but these studies do not seek to evaluate specific aquifer intervals or determine areas of the basin most appropriate for storage. This is important as the geological history of the basin presents several challenges that need to be assessed. The basin has very high geothermal gradients, particularly in the centre where they can exceed 50 °C/km (Madon and Jong, 2021). Injection of CO₂ into hot aquifers can be problematic as, under these conditions, the fluid density remains low, limiting storage capacity and increasing buoyancy pressure below the caprock. Many areas of the basin are also overpressured (Shariff, 1994), reducing the pressure space for injection but serving to increase the density of CO₂ for the same temperature conditions.

Every Miocene-age stratigraphic interval was evaluated in this study (from oldest to youngest: Groups K, J, I, H, F, E and D) (Fig. 1b). In addition to this, the Pliocene-age interval, Group B, was evaluated as the lack of hydrocarbons could be as a result of lack of charge rather than lack of reservoir, trap or seal presence. Older, Oligocene to Eocene stratigraphic intervals were not considered as part of this study as they are buried deeply across many regions of the basin and have not been penetrated by many wells elsewhere.

3. Data

The primary data used within this study is from hydrocarbon wells, including stratigraphic well tops, wireline logs and formation pressure test data. Stratigraphic well tops were available for 2435 Malay Basin wells. These tops consist of 5315 unique names, likely a consequence of different nomenclatures adopted by individual companies operating in the basin. These names were first remapped to a stratigraphic scheme often used within the basin using a dictionary implemented in a Python script, which can be found within a published dataset that accompanies this article (de Jonge-Anderson et al., 2025). This resulted in a more consistent dataset of 1004 wells (Fig. 1a) and 12 unique stratigraphic tops.

Wireline log (Modular formation dynamics tester (MDT) tool) formation pressure data were also analysed for 131 Malay Basin wells (Fig. 1a) and used to compile a database of formation pressure with depth for each aquifer (de Jonge-Anderson et al., 2025). Values were extracted from existing well reports where available, but to create a comprehensive database, a new analysis of raw, pressure-time MDT data was undertaken. To obtain accurate and consistent depths, deviation survey datasets were loaded into SLB Techlog software and used to calculate the true vertical depth below the seabed for each pressure test. Overpressure was then calculated as the difference between formation and hydrostatic pressure. Overpressure was noted within 50 wells and assigned to the relevant stratigraphic group to map overpressure distribution within each group.

Basin-wide seismic and temperature data were not used for this evaluation, and a full petrophysical evaluation of aquifer parameters was out-of-scope. However, we sought to incorporate these drawing on published literature on the basin. Basin-wide depth structure maps were digitized from PETRONAS (2022) and used within the gridding workflow as trend surfaces (see below). These were validated against regional

seismic data where available (see de Jonge-Anderson et al., 2024b for extent). A geothermal gradient map (Madon and Jong, 2021) was also digitized and used to create aquifer temperature maps. Finally, published porosity data (Madon et al., 1999) was utilised to generate porosity-depth trends (de Jonge-Anderson et al., 2025) across the basin (see below).

4. Methods

Several geological properties were mapped for each aquifer. These included depth, porosity, pressure, temperature, faults and CO₂ thermophysical properties, all calculated at the top of each aquifer (de Jonge-Anderson et al., 2025) (Fig. 2). A series of cut-offs were then applied to these maps to determine the optimal injection zones for each aquifer. SLB's Petrel and Techlog software was used for subsurface workflows including gridding and petrophysical analysis. Petrosys PRO was used for further gridding and data translation and ESRI's ArcPro was used for spatial data geoprocessing and visualisation. However, new Python routines (de Jonge-Anderson et al., 2025) were also developed to manipulate well tops, determine optimal zones and analyse clusters.

4.1. Creating depth structure surfaces

Depth structure surfaces for eight aquifer intervals were created by gridding stratigraphic well tops using the convergent interpolation algorithm available within Petrel E&P software with an additional input of a trend surface (Fig. 3). By including a trend surface, the gridding algorithm attempts to fit the input data (stratigraphic well tops) to the trend using a least squares approach and interpolates the output surface based on the residual. The trend surfaces themselves were generated by first georeferencing and digitizing, in ArcPro software, the contours and fault sticks from public-domain regional structure maps (PETRONAS, 2022) (Fig. 3b). Petrosys PRO was then used to grid these and exchange the data into a format compatible with Petrel E&P. The final depth structure surfaces were then created in Petrel E&P at 100 m by 100 m X and Y increment, before exporting as a raster file for subsequent analysis (Fig. 3c) (de Jonge-Anderson et al., 2025).

For depth maps of Groups B, E, H, I and J, a directly comparable surface was available from PETRONAS (2022). However, for depth maps of Groups D, F and K, no equivalent trend surface was available in PETRONAS (2022) and instead, trend surfaces from adjacent surfaces were used. In these instances, no major tectonic activity was known to affect the basin between the deposition of each Group, so the use of these trend surfaces (with true depths constrained by well tops) was considered reasonable. However, a major uplift and erosional event did affect the basin during the Late Miocene, which removed much of the younger Miocene aquifer intervals (Groups D, E, F and H) from the southeast of the basin and created a variable subcrop beneath the Intra-Late Miocene Unconformity (de Jonge-Anderson et al., 2024b). This was incorporated into the depth structure surfaces by removing the appropriate area in ArcPro software according to previously published subcrop limits (de Jonge-Anderson et al., 2024b).

4.2. Petrophysical evaluation

While a full petrophysical analysis was out of scope for this study, two, regional, NW-SE well correlations (Fig. 1a) were compiled and analysed in SLB Techlog software to illustrate typical aquifer characteristics and extract representative net-to-gross (NTG) ratio statistics for use in capacity estimates in subsequent sections.

Gamma Ray (GR) logs were used to determine the NTG ratio of each aquifer interval whereby a low GR reading is interpreted as indicative of a clean sandstone (as carbonates and evaporites are not present within this basin) and a high GR reading is interpreted as a mudstone. It was necessary to first normalise each GR log to account for different tool types and environmental corrections between wells. To achieve this, the

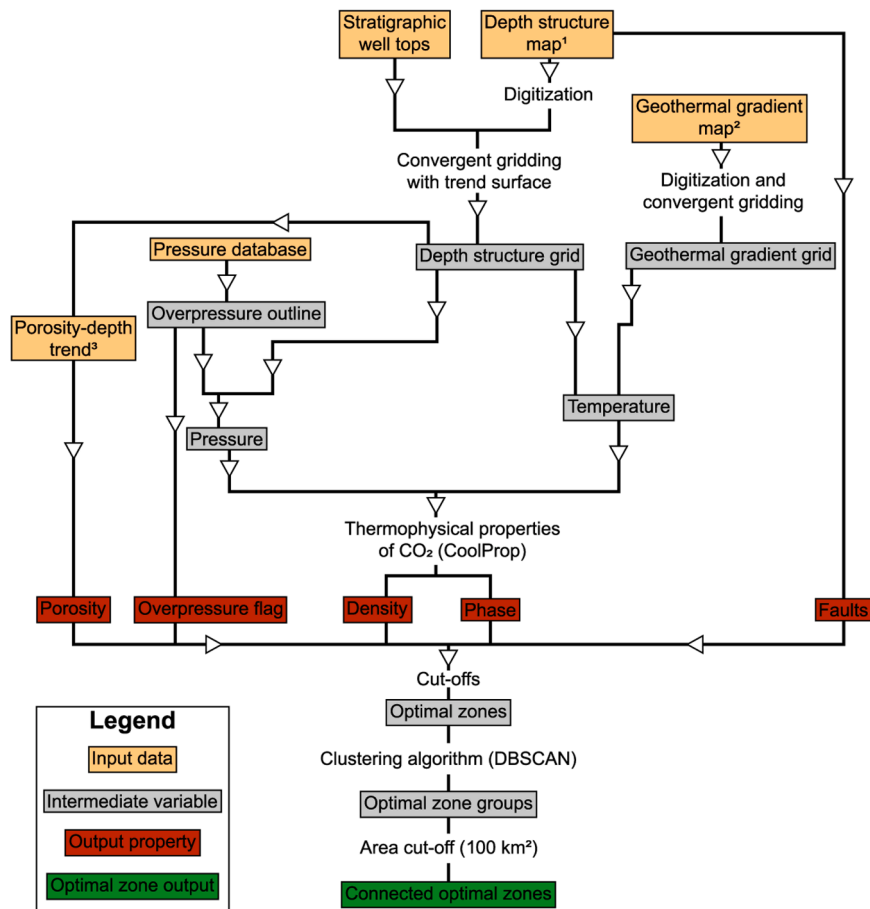


Fig. 2. Flowchart schematically illustrating the workflow created for this study. ¹PETRONAS (2022), ²Madon and Jong (2021), ³Madon et al. (1999).

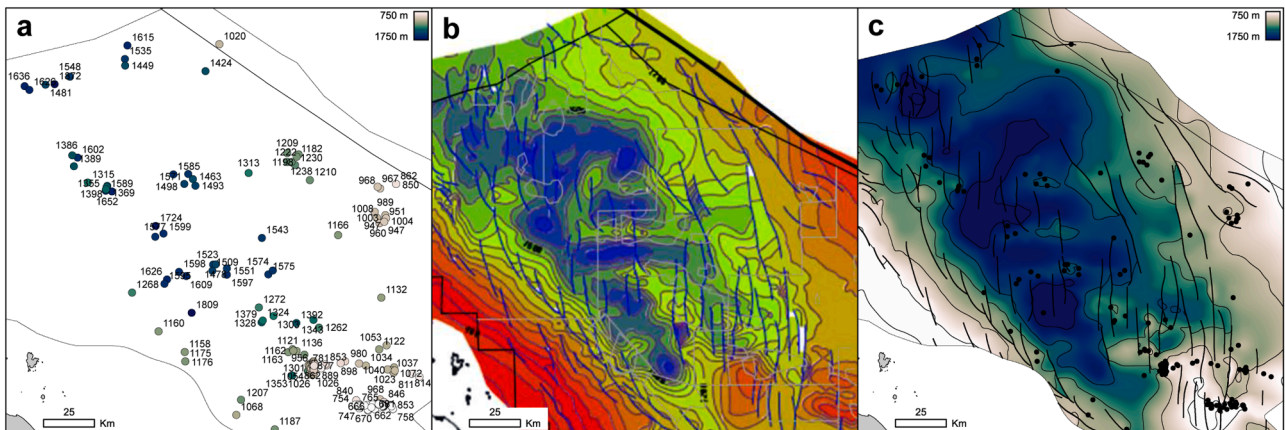


Fig. 3. Multi-panel figure illustrating the process of creating depth surfaces for a Malay Basin aquifer (Group E). a) wells coloured and labelled by depth of Group E, b) georeferenced regional depth surface from public-domain source (PETRONAS, 2022), c) final surface created by interpolating wells using b) as a trend surface.

following equation was used:

$$GR_{norm} = \frac{GR - GR_{min}}{GR_{max} - GR_{min}} \quad (1)$$

GR_{min} and GR_{max} were calculated at the 10th and 90th percentile of the data to avoid anomalous values and GR is initial reading. The NTG ratio was then calculated as the fraction of the gross aquifer interval with GR_{norm} values < 0.5 . This analysis was undertaken for twelve wells in the basin, and the mean and standard deviation of NTG ratio derived thereof (de Jonge-Anderson et al., 2025) were used to create normal

distributions for use in capacity analysis (see below)).

4.3. Porosity-depth model

Reservoir quality in the Malay Basin is strongly controlled by depositional facies and burial diagenesis, but these phenomena are extremely challenging to predict on a regional scale. Detailed geological modelling was out of scope for this study and is a challenging task when well penetrations are sparse. Here, we focused on the impact of burial diagenesis on the compaction of typical sandstones in the basin to

determine expected porosities at certain areas/depths under the assumption that sand-bearing intervals are present therein.

To undertake this, published porosity-depth data (Madon et al., 1999) were digitized and an exponential function fitted to it using a Python script (Fig. 4a), following the approach of Sclater and Christie (1980) and assuming a surface porosity of 45 %. This function was then applied to the depth surfaces outlined above (de Jonge-Anderson et al., 2025). The standard deviation of the dataset was also calculated, and upper and lower bounds were determined as one standard deviation above and below this fitted curve. The resulting trend shows rapid porosity decline, particularly in the uppermost 2000 m. At depths of around 1000 – 1500 m, this exponential curve is roughly linear, at around 1 % porosity decline per 100 m, which is in agreement with those previously described for the Malay and adjacent Pattani Basins (Madon et al., 1999). A lower porosity limit of 10 % is frequently used for GCS in saline aquifers (Chadwick et al., 2008; Ramirez et al., 2010; Callas et al., 2024), coincident with 3000 m according to this function.

4.4. Pressure, temperature and fluid modelling

The thermophysical properties of CO₂ were calculated using the CoolProp Python library (Bell et al., 2014). The temperature at the top of each stratigraphic group (de Jonge-Anderson et al., 2025) was first calculated using maps of depth and geothermal gradient and assuming a fixed seabed temperature of 24 °C (after Madon and Jong (2021)). The outlines of overpressured zones within each aquifer were mapped based on the pressure dataset described in Section 3 and for these, the pressure was calculated as 20 MPa/km. The rationale for picking this gradient is further described in subSection 5.3. For the remaining areas, hydrostatic conditions were assumed, and a gradient of 10 MPa/km was used. Maps of CO₂ phase and density (de Jonge-Anderson et al., 2025) were generated by performing equations of state calculations at every point on the depth, temperature and pressure surfaces (de Jonge-Anderson et al., 2025).

4.5. Optimal zones

4.5.1. Defining optimal zones

Many factors need to be considered to evaluate a saline aquifer for GCS, including those around maximising capacity/injectivity,

minimising containment risk and managing siting and economic constraints (Callas et al., 2024). This study does not attempt to consider all aspects required to identify the optimal GCS site but focuses only on subsurface properties. A fundamental aspect of a GCS site is that the aquifer should have sufficient porosity to store significant volumes of CO₂, and in a general sense, rocks with high porosity often have large pore throat radii, leading to high permeabilities, low capillary pressures and high injectivity. Screening is usually undertaken on the basis that the aquifer should have high porosity and permeability, but with the caveat that if permeability is too high, this could present challenges such as CO₂ runaway and/or lower storage efficiency. In this work, we imposed a lower porosity cut-off of 10 %, which aligns with a recent study on screening saline aquifers for CGS (Callas et al., 2024). This porosity corresponds approximately to permeabilities of around 100 mD and higher (Fig. 4b).

The treatment of faults within GCS screening workflows is complex. Faults can pose a containment risk, if permeable, but the risk will depend on the properties of the damage zone around the fault and the geometry of the fault (Wibberley et al., 2008). However, permeable faults could also be considered a positive factor for GCS, alleviating pressure buildup in the reservoir. They can also pose a risk of induced seismicity, though this risk will depend on the stress regime of the basin and the specific fault, amongst other factors (Cheng et al., 2023). On the other hand, sealing faults have historically provided effective trapping mechanisms for hydrocarbon accumulations (Spencer and Larsen, 1990). In this work, faults and zones of higher fault intensity are treated as a risk, and thus optimal zones are limited to those areas that are at least 2 km away from the nearest mapped fault. The use of a 2 km limit setback distance is based on work undertaken in the Gulf of Mexico (Callas et al., 2024), but more detailed fault-seal and geomechanical analyses (Karolytè et al., 2020; Wu et al., 2021; Snippe et al., 2022; Rizzo et al., 2024; Ramachandran et al., 2024) could be used to reduce or increase this value.

Areas of overpressure were also excluded when mapping optimal zones. If CO₂ was injected into an overpressured aquifer, the formation pressure would rise to reach fracture pressure quicker than it would for a normally pressured aquifer. This would ultimately constrain the storage capacity, require costly pressure relief measures and potentially introducing unwanted geomechanical effects. However, as we map the outline of overpressure and assume a constant gradient of 20 MPa/km (the maximum we observed from well data), we likely overlook some

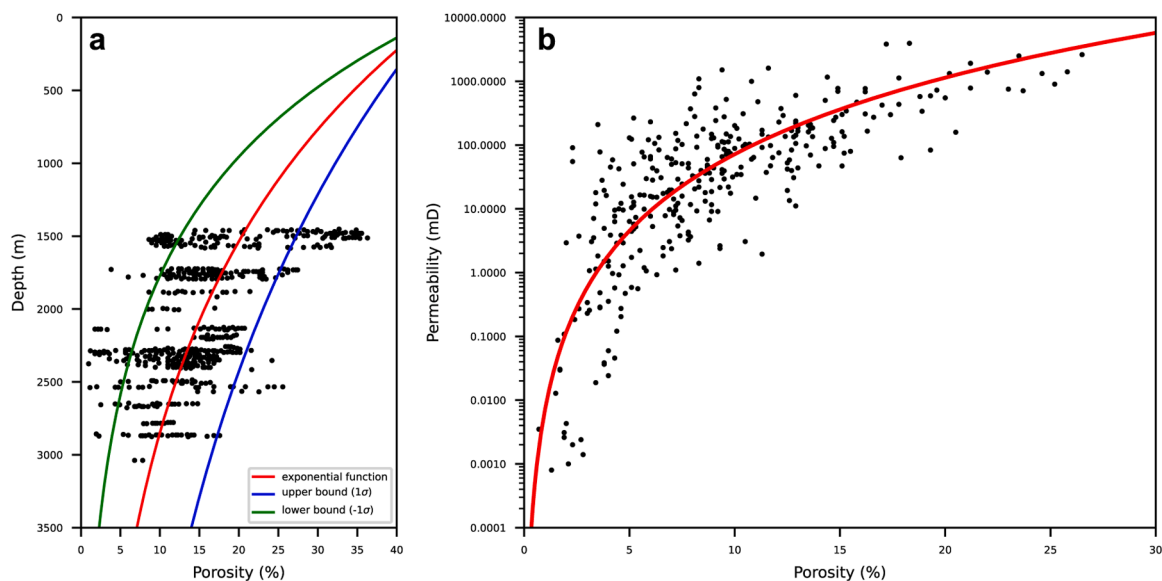


Fig. 4. a). Crossplot of sandstone porosity versus depth (after Madon et al., 1999) with three trendlines. An exponential function (after Sclater and Christie, 1980) was fitted to the scatter data assuming a porosity at seabed of 45 %. The lower and upper bounds represent one standard deviation above and below the trendline and are utilised in the capacity modelling in subSection 4.5.2. b) Crossplot of sandstone porosity versus permeability derived from petrophysical logs.

areas where the overpressure is less extreme, and CO₂ injection might be possible.

Specific constraints were also placed on the modelled thermophysical properties of CO₂. An optimal region must favour CO₂ as a supercritical phase with high density. The high temperatures present in the Malay Basin aquifers suppresses the modelled CO₂ density at a given depth and pressure. Less dense CO₂ would lead to reduced capacity and more buoyancy pressure on caprocks, potentially compromising retention. To account for this, a lower density cutoff of 300 kg/m³, was applied to ensure that optimal zones did not include regions where very light CO₂ might be injected. This cut-off is consistent with the lowest CO₂ density permitted in a recent saline aquifer screening study (Callas et al., 2024).

The final step was to place an area constraint on each individual optimal zone (Fig. 5). To do this, a concept of “connected area” was introduced where any segments of optimal zones with areas smaller than this connected area were excluded from the screening result (assumed to be too small for serious consideration as GCS targets). This was undertaken by first implementing a DBSCAN clustering algorithm (de Jonge-Anderson et al., 2025) available within the scikit-learn Python library (Pedregosa et al., 2011). The DBSCAN algorithm clusters data points based on their density, grouping points that are closely packed within a specified radius. The main advantage of using such an algorithm over other clustering algorithms (e.g. k-means) is that DBSCAN can independently identify the number of clusters to be found, and these clusters can have arbitrary shapes and sizes. The two, key, user-defined parameters are the radius, and the minimum number of samples required within that radius for a data point to be considered a core point in the formation of a cluster (Pedregosa et al., 2011). These were defined as 100 and 5 respectively, following the visual inspection of multiple iterations of clustering using various parameter values. The algorithm was effective in grouping connected regions of optimal zones and assigning each a specific label (Fig. 5b). Following this, the total area of each group was calculated and any group with an area <100 km² was excluded. While this cut-off was not validated by modelling in this study, it is considered a reasonable representation of the footprint of a typical CGS project/licence.

The creation of optimal zone maps was undertaken using a Python script (de Jonge-Anderson et al., 2025). In addition to optimal zones, sub-optimal zones were also calculated. For these zones, less stringent

criteria were applied (lower porosity cut-off of 6 % (equivalent to 10 mD permeability and greater), lower CO₂ density cut-off of 100 kg/m³, supercritical phase and at least 100 m distance from a mapped fault). These areas are shown in the map figures for comparison, but volumetric analysis was not undertaken.

4.5.2. Estimating volumetric storage capacity

The total storage capacity of each optimal zone was also calculated. There has been much discussion around determining accurate capacity estimates for GCS. Basin-scale estimates are usually made by considering the pore volume of the aquifer region, or structural closure with the dynamic behaviour of the aquifer approximated via an efficiency factor (van der Meer, 1995; Goodman et al., 2011; Wang et al., 2013; Bachu, 2015). Ultimately, full physics reservoir simulations (Hosseini et al., 2024), or reduced complexity models (Gasda et al., 2009; de Jonge-Anderson et al., 2024a) can produce more accurate estimates, but these studies are usually undertaken once a storage site has been selected and matured. In this work, the aim was not to calculate precise values of storage capacity but to evaluate the relative potential of each aquifer in a way that honours the data used within this work (depth, compaction trend, fault lines, modelled CO₂ properties). To implement this, a probabilistic, Monte Carlo approach was used consisting of 1000 simulations.

A well-established equation for calculating storage capacity was used (after Goodman et al., 2011):

$$M_{CO_2} = A * h * NTG * \phi * (1 - S_{w_{irr}}) * E * \rho_{CO_2} \quad (2)$$

Where A is the area of the optimal zone, h is the thickness, NTG is the net-to-gross ratio, ϕ is porosity, $S_{w_{irr}}$ is irreducible water saturation and E is the storage efficiency factor. Values for h, NTG, ϕ , $S_{w_{irr}}$, E and ρ_{CO_2} were obtained from randomly sampling normal distributions of those properties with the mean and standard deviations constrained from analysis of wells or property maps generated in this study where possible (Table 1). Mean values of 2 % (Hasbollah et al., 2020) and 27 % (de Jonge-Anderson et al., 2024a) were adopted for E and $S_{w_{irr}}$ respectively.

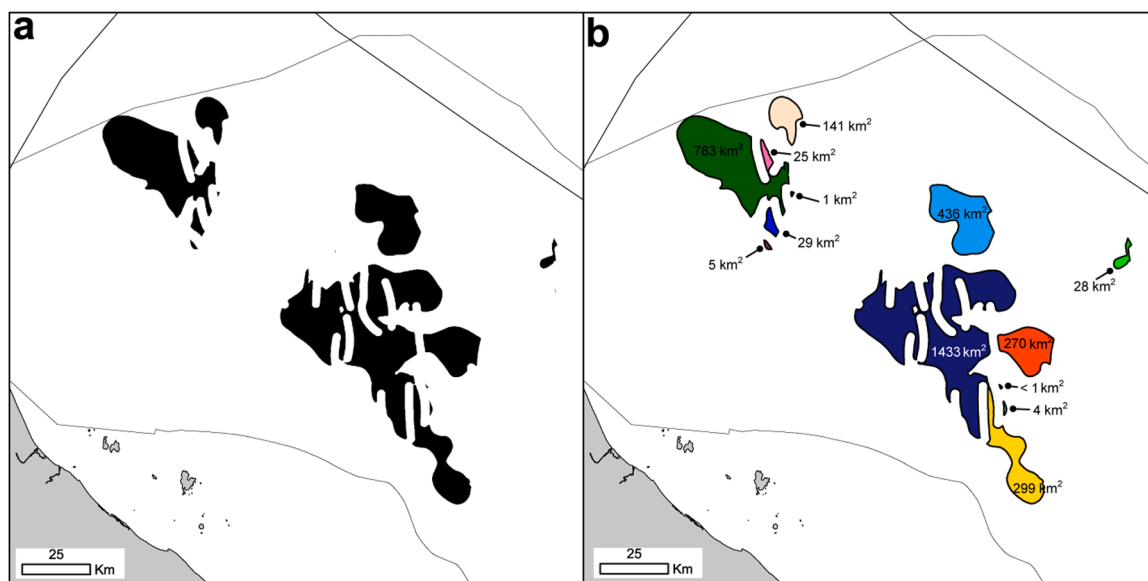


Fig. 5. Multi-panel figure illustrating the process of determining clusters of optimal zones and calculating connected areas. a) map of northern Malay Basin where black colour indicates an optimal zone output from the process described in subSection 4.5.1. b) results of cluster analysis where groups of connected optimal zones are assigned to an individual colour. The area of each group is then calculated and those with areas <100 km² are discarded in subsequent analysis.

Table 1
Variables used within capacity estimates grouped by source.

| Derived from well petrophysics | Extracted from property maps | Representative literature values |
|--------------------------------|---|----------------------------------|
| Net-to-gross (NTG) | Porosity (ϕ) | S_{wirr} |
| Thickness (h) | CO ₂ density (ρ_{CO_2}) | E |
| | Area (A) | |

5. Results

5.1. Petrophysics

Analysis of the two well correlations compiled for this study (Fig. 6, with location of sections shown in Fig. 1a) suggests that there are many candidate sandstone-bearing intervals across the Malay Basin for GCS, with both stratigraphic and spatial variations in NTG ratio. The oldest aquifer evaluated within this study, Group K, consists of thick (up to 50 m) sandstones underlying a mudstone, with NTG ratios between 0.30 and 0.59 (Fig. 6). Group J is also predominantly sand-rich, with NTG up to 0.61, but it is thinner than Group K. Group I represents a thick shallow marine sequence, but with thinner sandstone beds and low NTG ratios between 0.04 and 0.26. Groups H and F also appear limited in sandstone development with NTG ratios of 0.12 on average. Group E is an important hydrocarbon reservoir interval, with NTG ratios of up to 0.42,

averaging at 0.27. Group D also contains some well-developed sands (e.g. 0.3 NTG ratio in N-1), but these appear to be patchy, with some wells showing limited sand development (e.g. 0.10 NTG ratio in ID-1 and TG-2). The shallowest reservoir interval, Group B appears to contain many thin sandstone intervals averaging at 0.17 NTG ratio, however, this interval lacks significant hydrocarbon accumulations and is usually only partly logged, resulting in greater uncertainty than older groups.

5.2. Depth and porosity

The shallowest aquifer, Group B lies mostly between 280 and 650 m depth below mean sea level (mostly < 70 m (GEBCO Compilation Group, 2023)), with an average of 444 m (Fig. 7a) and in contrast with deeper intervals in the basin, there are only small changes in depth across the basin. At these depths, modelled sandstone porosities are 36.0 % (median value) \pm 2.5 % (one standard deviation), representing a significant retention of primary porosity. More structural variation can be observed within the underlying Group D, which is ~ 1300 m deep in the centre of the basin, rising to <500 m deep at the margins (Fig. 7b). At these depths, modelled sandstone porosities are 26.7 % \pm 5.0 % (Fig. 4a). This aquifer is also absent in the southeast of the basin following truncation beneath the intra-Late Miocene Unconformity (de Jonge-Anderson et al., 2024b). Groups E and F (Fig. 7c and d) show a similar pattern but are notably deeper in the centre of the basin, around 1700 m and 2000 m respectively. However, reasonable porosity is still expected to be

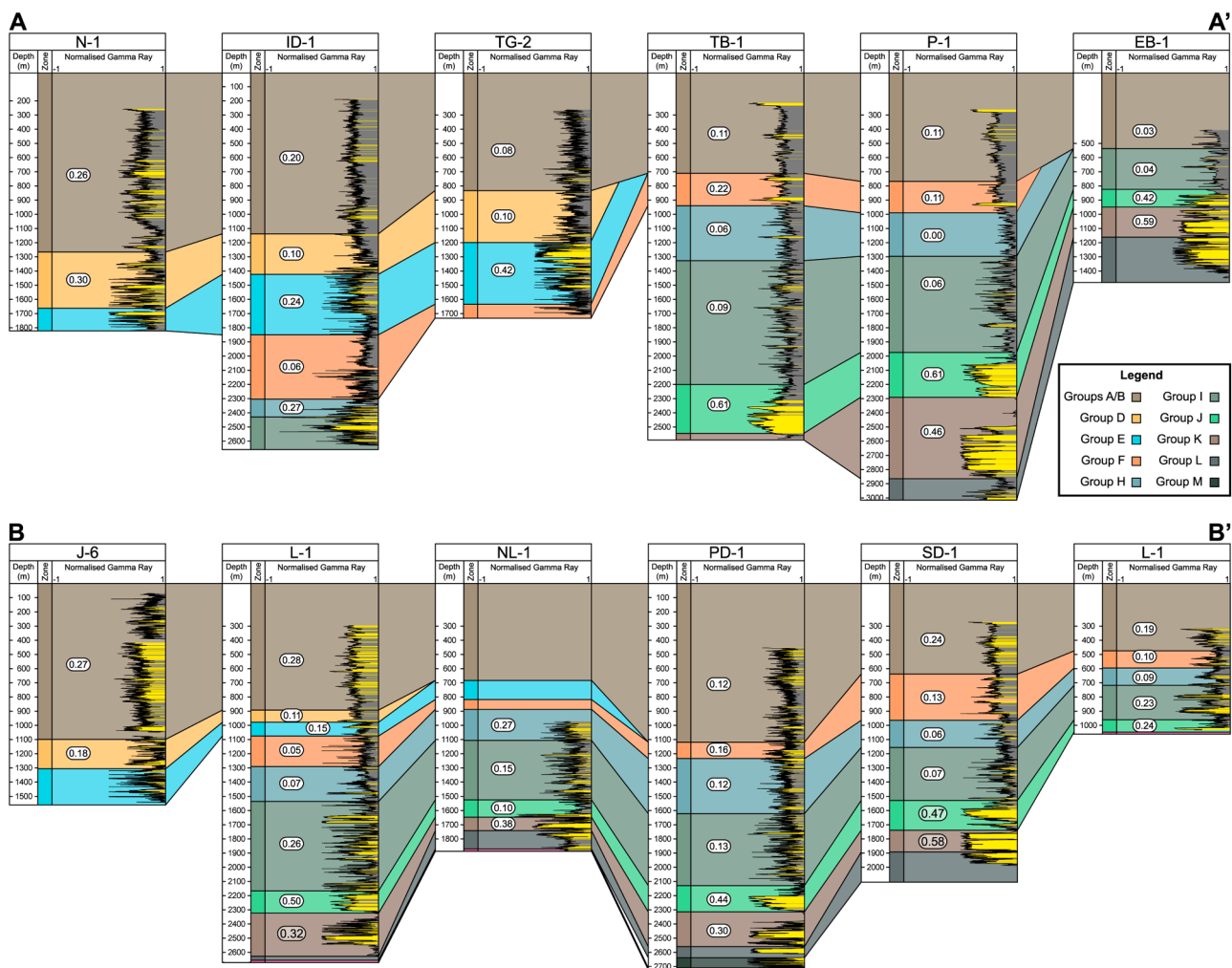


Fig. 6. Two NW-SE oriented well correlations displaying normalised Gamma Ray logs coloured whereby values of 0.5 and less are yellow (interpreted as sandstone). Net-to-gross ratios are labelled for each aquifer interval and calculated as the fraction of sandstone to mudstone for that interval. Please refer to Fig. 1a for the location of the correlations.

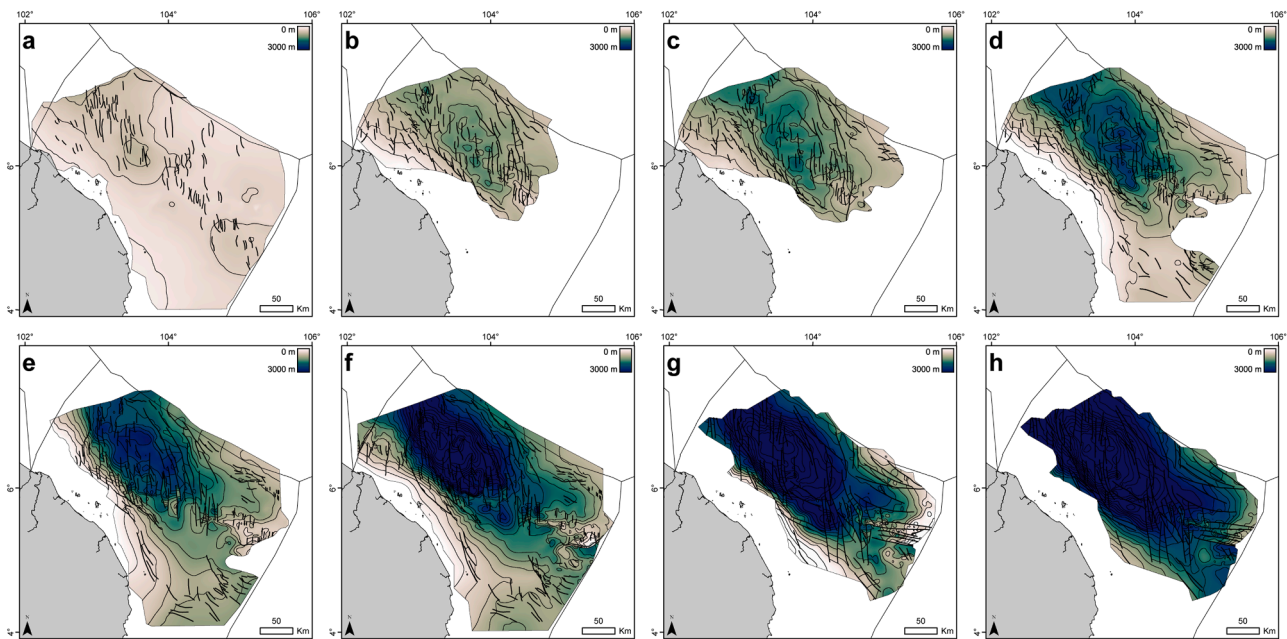


Fig. 7. Multi-panel plot showing the top depth (in true vertical depth subsea) structure of the eight aquifers selected for analysis in this study. The eroded sections in the southeast of the basin are drawn after the Pliocene subcrop map within de Jonge-Anderson et al. (2024). The maps were created by gridding stratigraphic well tops using an algorithm that fits the surface trend to that of a guide surface. The guide surfaces and fault polylines were taken from PETRONAS (2022). a) Group B, b) Group D, c) Group E, d) Group F, e) Group H, f) Group I, g) Group J, h) Group K.

preserved at these depths, with Group E modelled porosities of $24.5 \% \pm 4.7 \%$ and Group F modelled porosities of $26.1 \% \pm 7.9 \%$ (Fig. 4a). There is less erosion of these groups in the southeast, particularly Group F, which is only absent in an area near the maritime border with Indonesia.

Within the groups described thus far there has been limited fault influence on depth structure, a reflection of relatively minor tectonic activity during the upper Miocene to Pliocene. In Groups H and below (Fig. 7e-h), faults appear to have more control over the depth structure. This is notable along the western margin hinge zone and central parts of the basin where north-south faults create a series of horsts and grabens. Intervals within Group F and older are buried significantly in the centre

of the basin. By Group H, modelled porosity is likely $< 15 \% \pm 7.9 \%$ in the centre of the basin and by Group I and older, it is likely $< 10 \% \pm 7.9 \%$ in the centre. The oldest aquifer studied, Group K is > 5000 m deep in the centre of the basin (Fig. 7h), corresponding to $< 5 \% \pm 6.5 \%$ porosity (Fig. 4a).

5.3. Pressure distribution

Some general observations are made from a cross plot of formation pressure with depth, compiled from 131 wells, and coloured by aquifer interval (Fig. 8a). Formation pressure, and thus overpressure tends to increase with depth below the seabed, though the pattern is complex.

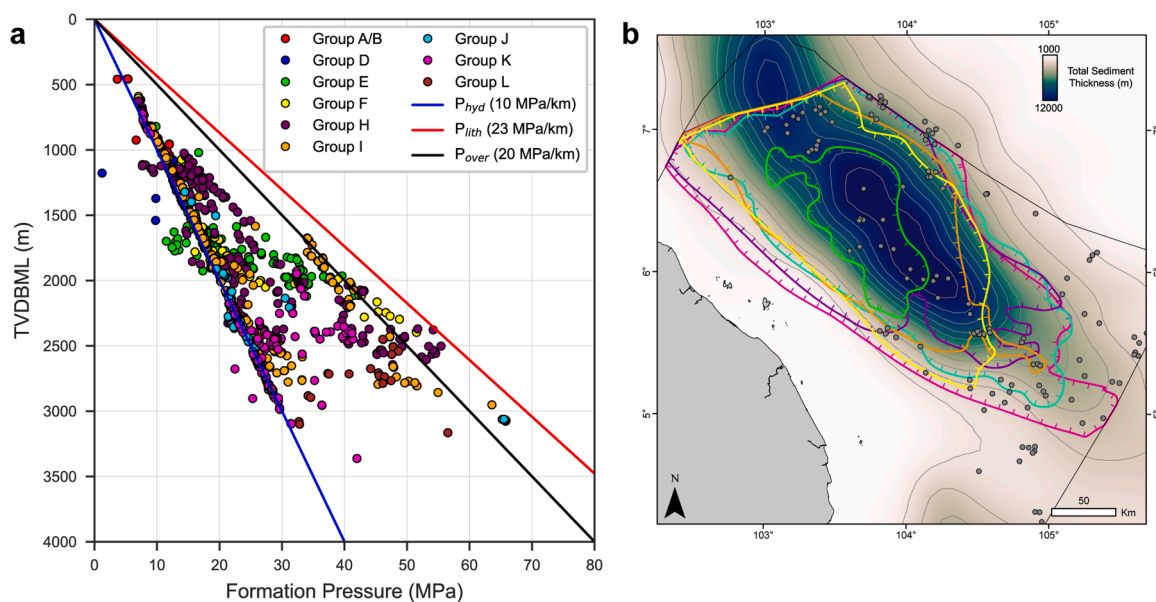


Fig. 8. a). Crossplot of formation pressure versus true vertical depth below the mudline (seabed), coloured by aquifer. **b)** Map showing the outline of overpressured regions for each aquifer based on analysis of the same data as shown in a). The colours used for each aquifer are identical to those shown in a).

The Pliocene-Pleistocene Groups A and B exhibit no overpressure and position close to the hydrostatic pressure.

Moderate overpressure starts at around 1000 m depth, specifically within Group H (Fig. 8a). The presence of overpressure in the Malay Basin has been well documented, attributed to disequilibrium compaction (Madon, 2007) further augmented in areas by localised hydrocarbon generation within organic-rich intervals (Tingay et al., 2013).

Group H exhibits some of the largest overpressures in the basin, notably around 2500 m depth, where formation pressure approaches lithostatic pressure (Fig. 8a). At around 1750 m, rapid increases in formation pressure within younger Groups E and F can be observed. Formation pressure quickly reaches the 20 MPa/km gradient before aligning approximately with this, suggesting the rapid increase is indicative of a transition zone. Formation pressures within Group I also adhere to this 20 MPa/km gradient, though the presence of a transition zone is less clear. Deeper and older stratigraphic intervals generally show less clear trends in pressure, with various test points plotting between hydrostatic and lithostatic pressure gradients.

The spatial distribution of overpressured regions displays some alignment with the total sediment thickness in the Malay Basin (Fig. 8b), implying that disequilibrium compaction is the dominant cause of overpressure generation at a regional scale. The youngest aquifer exhibiting any overpressure (Group E), is overpressured only in the northwest of the basin. The extent of overpressured region increases with age of aquifer, although the southwest and northwest limits for Groups F, H, I, J and K are quite similar (Fig. 8b), likely due to rapid overpressure development associated with steep basin margins (Fig. 7). The southeast margin of the basin exhibits more complex overpressure spatial distributions, with the pattern influenced by local highs, particularly apparent for Group H (Fig. 8b).

To extract an overpressure gradient for use within modelling work, a gradient of 20 MPa/km was chosen, and this was used to model pressure for the entire region in which overpressure was noted (Fig. 8b). This gradient is well aligned with an interval of Fig. 8a between 1750 m and 2500 m. However, the use of this trend presents some limitations, notably overestimating overpressure in the complex transition zones.

5.4. Final property maps

Maps of depth, porosity, pressure and temperature, fault intensity and CO₂ thermophysical properties were created for each aquifer. Fig. 9 illustrates an example for Group J, with raster grids for the other aquifers presented in de Jonge-Anderson et al. (2025). Optimal zones were calculated by applying the cut-offs described above to porosity, CO₂ property and fault maps, leading to classifications of optimal (green), sub-optimal (yellow) and non-viable (grey) areas for each aquifer (Fig. 10).

The areal extent of the optimal zones for GCS exhibits a pattern whereby the extent initially increases with the age of the aquifer (Fig. 11, Table 2). Group B is at shallow burial depth across the basin (Fig. 7a) and at these depths, sandstone aquifers are likely to have retained significant porosity (Fig. 4a), but the modelled CO₂ densities are very low, with a median value of 87.5 kg/m³ ± 32.6 kg/m³ (one standard deviation). This is a consequence of low formation pressures and high geothermal gradients and results in no optimal zones and only small areas of sub-optimal zones being calculated (Fig. 11a). Similarly, Group D aquifers, being buried no greater than 1500 m (Fig. 7b), likely exhibit high porosities (Fig. 4a) but optimal zones are constrained by modelled CO₂ densities and restricted to local depressions in the centre of the basin (Fig. 11b). The median modelled value for this aquifer is 238 kg/m³ ± 76.0 kg/m³, which itself is beneath the lower cut-off selected for determining optimal zones. This results in the smallest areal coverage, at 3348 km², of any optimal zones highlighted (Table 2).

Group E is at depths sufficient to exceed the 300 kg/m³ density cut-off over much of the northwest of the basin, but the modelled porosity within some deeper parts drops to less than 15 %, represented as non-optimal zonation (Fig. 11c). Starting with Group F, the optimal zones shift to the margins of the basin (Fig. 11d–h), as the aquifers in the central part are too deep to retain significant porosity. For Groups F and H, few optimal zones are found in the centre, but the porosity is mostly greater than 10 %, designated as non-optimal zones (Fig. 11d–e). For Groups I, J and K, porosity in the centre of the basin is too low (< 10 %) to be considered realistic for GCS (Fig. 11f–h). These aquifers rise to relatively shallow depths on the flanks of the basin, passing the 300 kg/m³ CO₂ density cut-off ~ 60 km from the coastline.

The maximum areal extent of optimal zones is observed within

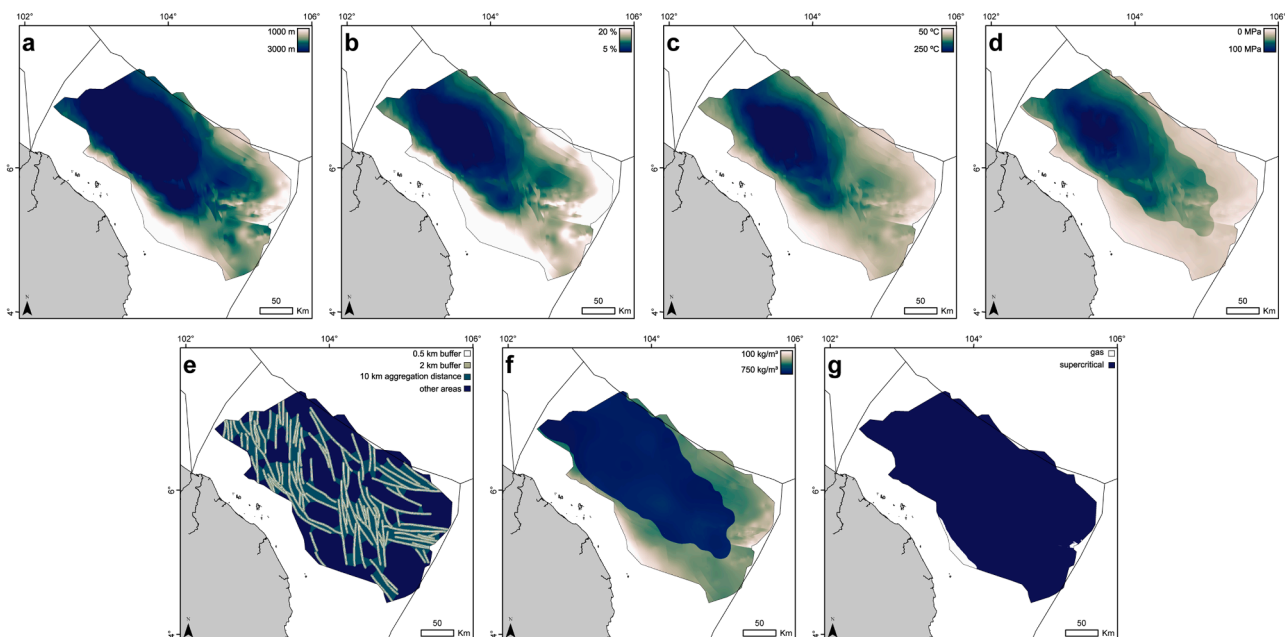


Fig. 9. Multi-panel plot showing an example of the various GCS property maps derived during this study. The example shown is for the Group J aquifer. a) depth, b) porosity, c) temperature, d) pressure, e) fault intensity, f) CO₂ density, g) CO₂ phase.

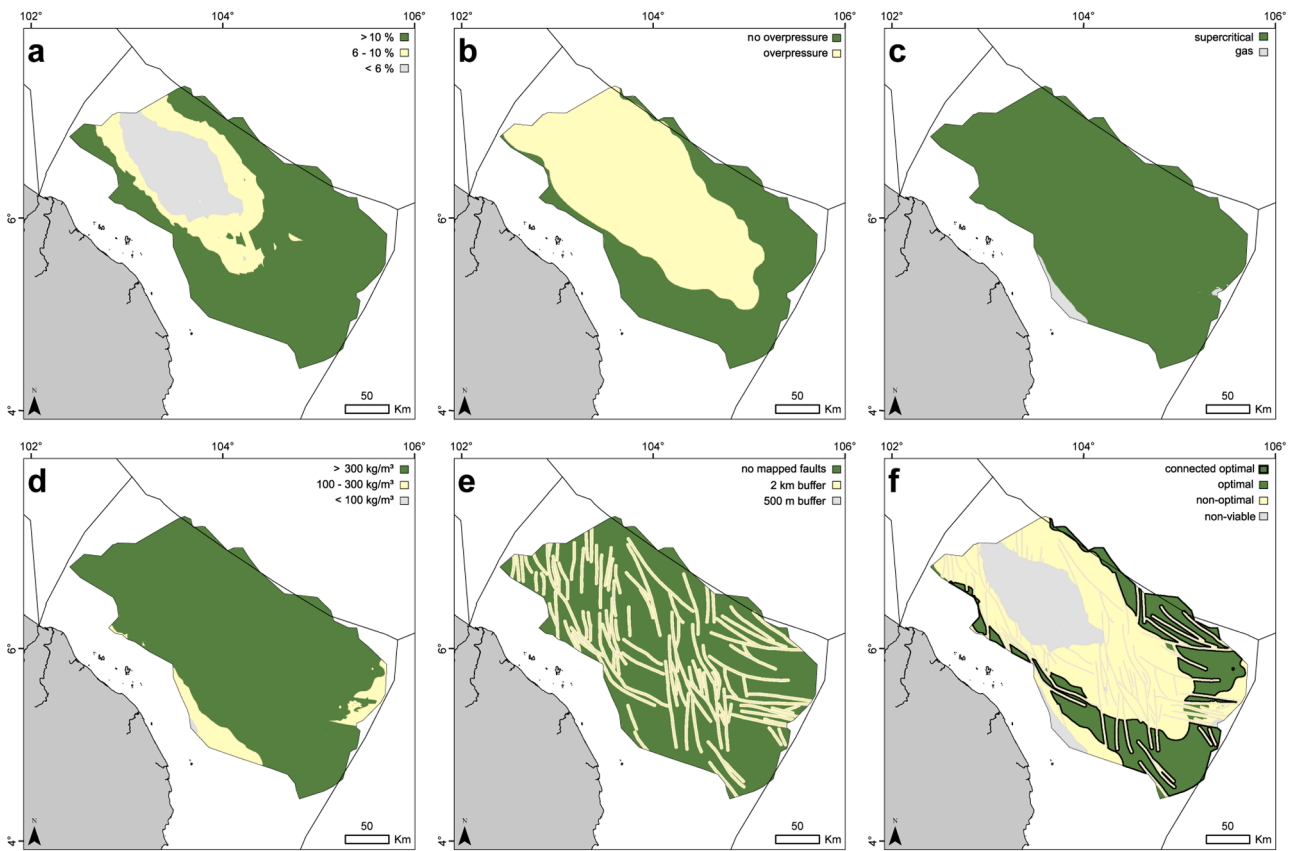


Fig. 10. Multi-panel plot showing various property maps for Group J and highlighting the optimal areas (green), non-optimal areas (yellow) and non-viable areas (grey) following the cut-offs described in subSection 4.5.2. a) porosity, b) overpressure flag, c) CO₂ phase, d) CO₂ density, e) fault intensity, f) optimal zones.

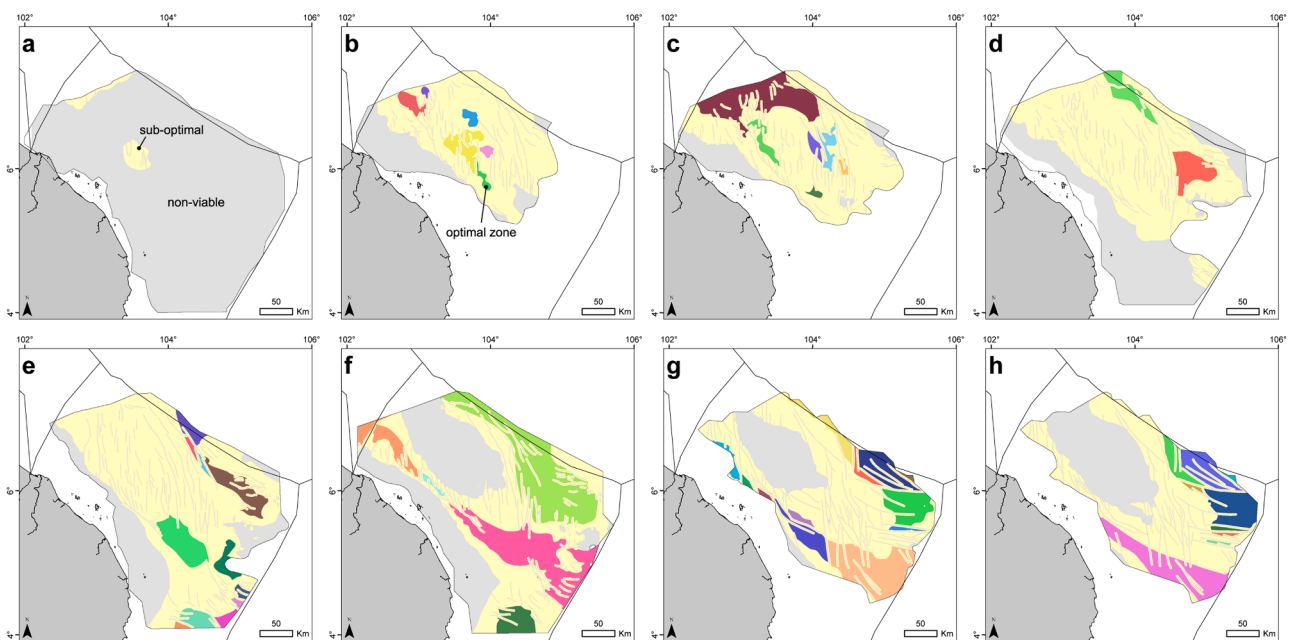


Fig. 11. Multi-panel plot showing the optimal, sub-optimal and non-viable zone maps for each aquifer. The optimal zones are coloured according to the output of the cluster model. a) Group B, b) Group D, c) Group E, d) Group F, e) Group H, f) Group I, g) Group J, h) Group K.

Group I (Fig. 11f, Table 2), as this interval is well suited in that it is sufficiently buried to possess the pressure and temperature needed for a dense CO₂ phase, but not too deep (over most of the basin) that primary porosity is reduced significantly. The areal extent of older aquifers is

significantly more restricted, with optimal zones being restricted to a band in the southeast corner of the basin.

Table 2

Summary of the optimal zones, average properties within them and the mean volumetric storage capacity for each aquifer. Corresponding capacity distributions are shown in Fig. 12. \bar{x} : arithmetic mean, σ : standard deviation, M: median.

| Group | Input | | | | Output |
|-------|---|------------------------------------|--|-------------------------------------|-------------|
| | Calculated within optimal zones | | | Fixed, per group | |
| | Area of optimal zone (km ²) | Porosity (%), $\bar{x} \pm \sigma$ | CO ₂ density (kg/m ³), $\bar{x} \pm \sigma$ | Thickness (m), $\bar{x} \pm \sigma$ | |
| B | No optimal zones | | | 162 ± 12 | 0.17 ± 0.09 |
| D | 3348 | 22 ± 1 | 313 ± 11 | 287 ± 262 | 0.16 ± 0.09 |
| E | 13,894 | 21 ± 2 | 336 ± 30 | 354 ± 280 | 0.27 ± 0.14 |
| F | 18,108 | 22 ± 2 | 340 ± 41 | 449 ± 415 | 0.12 ± 0.06 |
| H | 22,290 | 23 ± 2 | 327 ± 29 | 393 ± 294 | 0.12 ± 0.10 |
| I | 24,924 | 20 ± 3 | 362 ± 37 | 610 ± 264 | 0.13 ± 0.08 |
| J | 12,898 | 18 ± 3 | 394 ± 40 | 272 ± 118 | 0.42 ± 0.17 |
| K | 10,643 | 17 ± 4 | 403 ± 42 | 383 ± 176 | 0.44 ± 0.13 |

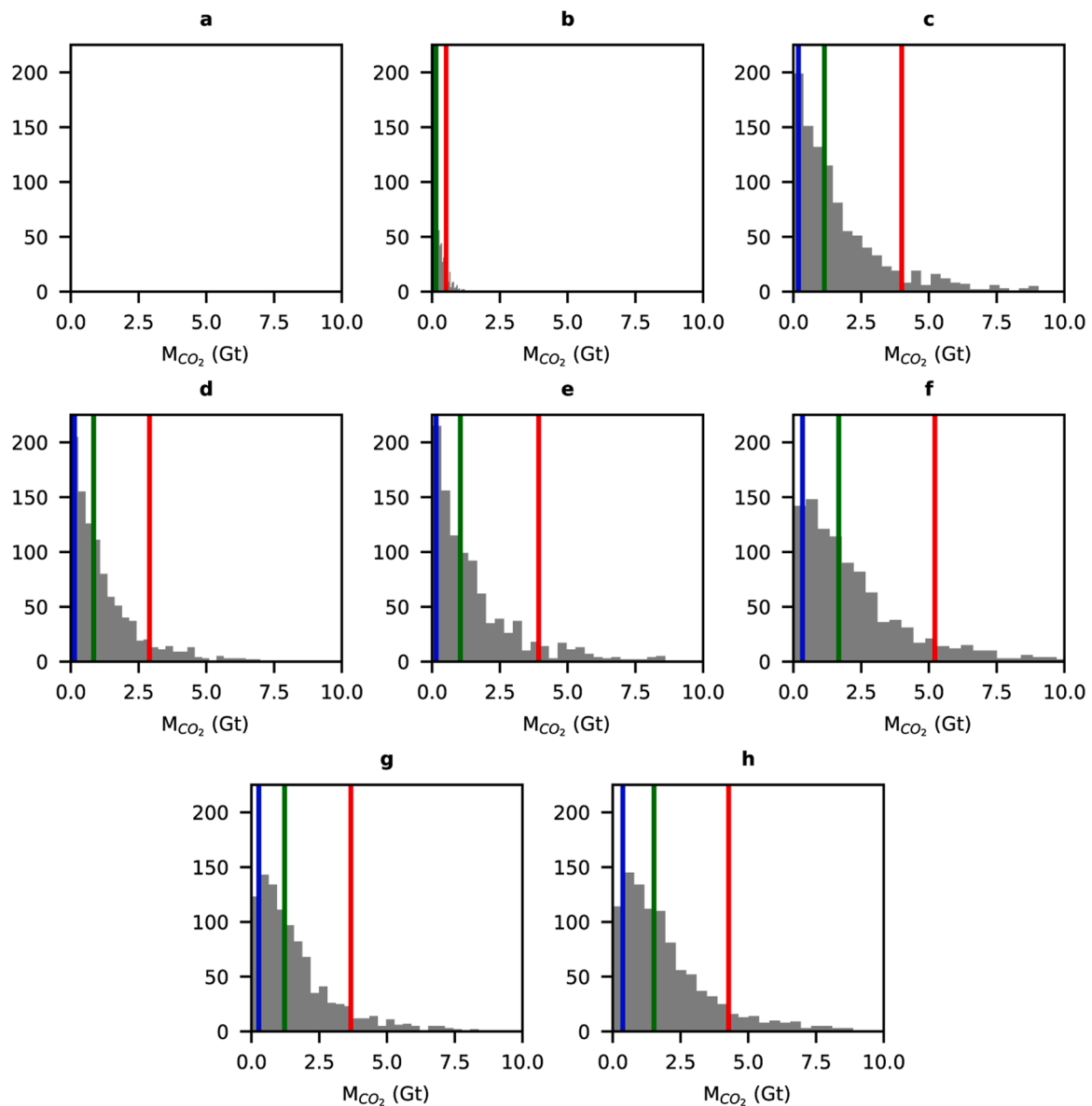


Fig. 12. Multi-panel plot illustrating the results of the Monte Carlo simulations to derive truncated normal distributions of volumetric storage capacity for each aquifer within the optimal zones only. The blue, green and red vertical lines represent the 10th, 50th and 90th percentiles respectively. a) Group B, b) Group D, c) Group E, d) Group F, e) Group H, f) Group I, g) Group J, h) Group K.

5.5. Volumetric capacity

Probabilistic calculations show that there is substantial storage capacity within the Malay Basin, with a P50 capacity of 7.6 Gt (Table 2). However, the associated uncertainty is high, reflected by the high P10 (24.5 Gt) and low P90 capacity (1.44 Gt), underscoring the need for further refinement. Optimal zones within Group D present the smallest CO₂ storage capacity (Table 2, Fig. 12b), owing to their limited areal extent (Fig. 11b), low modelled CO₂ densities and relatively low NTG formation (Table 2; Fig. 6).

Optimal zones within Group E are also fairly limited in areal extent but their higher NTG characteristics (Table 2; Fig. 6) and denser modelled CO₂ (Table 2), result in a higher storage capacity. The P50 value calculated was 1.14 Gt, but the aquifer's optimal zones are potentially capable of storing several gigatonnes of CO₂ (Table 2, Fig. 12c).

Groups F, H and I represent low NTG but volumetrically important aquifers in the basin. Optimal zones within Group F are also limited in areal extent but are associated with high modelled densities of CO₂ (Table 2). Group H is a thinner aquifer, but given the greater extent of optimal zones, and high CO₂ densities modelled within them, offers a large storage capacity of (Table 2, Fig. 12e). Group I is the thickest aquifer (> 600 m on average) and contains the greatest areal extent of optimal zones (Table 2, Fig. 11f), resulting in it possessing the largest storage capacity observed in this study (Table 2).

The two oldest aquifers evaluated, Groups J and K, are higher NTG (Fig. 6, Table 2), but thinner and with fewer optimal zones than Groups F, H and I (Fig. 11g and h). Optimal zones within Group J offer the third lowest storage capacity. Group K, despite containing the third lowest areal extent of optimal zones, presents the second largest P50 storage capacity at 1.52 Gt, likely a consequence of the higher average thickness (than Group J) and high NTG (Table 2, Fig. 12g and h).

6. Discussion

6.1. Regional significance

The findings presented herein indicate that optimal zones for GCS are widely distributed across the Malay Basin and across various saline aquifer targets. This result is significant in that there has been a substantial recent acceleration in CCS screening and development activity in Malaysia. The government has set ambitious CCS targets, with the Ministry of Economy's National Energy Transition Roadmap proposing that by 2030, three CCS hubs should be developed (two in Peninsular Malaysia and one in Sarawak) delivering 15 Mtpa, rising to 40 – 80 Mtpa by 2050 (Ministry of Economy (Malaysia), 2023). In addition, there have been indications that Malaysian GCS sites could be used to store CO₂ imported from neighbouring countries, notably Japan (Reuters, 2023).

While the most advanced GCS project in Malaysia is in waters offshore Sarawak, Peninsular Malaysia has gained recent attention, with several agreements to explore the potential in both the Malay and Penyu Basins (TotalEnergies, 2023; Storegga, 2024). Both basins are attractive regions for GCS due to their proximity to populous and industrial areas of the Peninsular Malaysia coast, but the presence of undeveloped high-CO₂ gas discoveries in the Malay Basin provides an added impetus for GCS development. Gas discoveries with high concentrations (up to 75 mol%) of naturally occurring CO₂ have been found in the northern part of the Malay Basin (Madon et al., 2006) but have remained undeveloped to date due to the costs associated with processing and disposal of the CO₂. A cluster of these fields (Bujang, Inas, Guling, Sepat and Tujoh: BIGST) will be developed with GCS to permanently dispose of the CO₂ in the coming years (PETRONAS, 2024a). As the BIGST cluster of fields is located in the northern part of the basin, the results presented in this study suggest that it is aquifers within Group D and Group E that would be best suited to GCS for this purpose (optimal zones being

present and immediately adjacent to the BIGST cluster of fields).

A CCS hub is also in the early stages of development in the southern part of Peninsular Malaysia, near Pahang (PETRONAS, 2024b). The Malay Basin is ~ 200 km from this stretch of coastline, and recent activity has focused on the appraisal of the Penyu Basin (Storegga, 2024), which was out of scope for this study. Optimal zones within Groups H and I are present in the far southeast of the Malay Basin and one could speculate at continuation of this trend further south, but the Penyu Basin is in many ways a distinct basin with a less developed Miocene-Pliocene sequence and the presence of thick, syn-rift Eocene-Oligocene sequences at reasonable depths of burial for porosity to be preserved (Madon et al., 2019).

6.2. Importance of stacked reservoirs

Our results also highlight the volumetric storage capacity within thick, but low NTG aquifers, notably middle Miocene aquifers (Groups F-I) (Figs. 1b and 6), which according to this study's results, are optimally located over a large area of the basin (Fig. 11) and offer significant storage capacity (3.55 Gt (P50)) (Table 2) of which around half is within Group I (1.67 Gt (P50)) (Table 2).

Low NTG intervals consisting of stacked sandstones interbedded with mudstones can offer several benefits to GCS. The increased vertical heterogeneity can lead to more tortuous migration pathways and greater contact time between CO₂ and water, ultimately supporting further dissolution and residual trapping. This effect has been observed in GCS studies focused on fluvial successions with heterogeneous architectures (Sun et al., 2023). There could also be added injectivity and pressure management benefits, notably in reducing the risk of large-scale pressure buildup when compared to injection into a single aquifer (Wijaya et al., 2024). However, increased heterogeneity can also present un-desirable effects, such as erratic pressure behaviour and/or injectivity constraints (Jin et al., 2014; Sun et al., 2023).

Some recent studies have suggested that low NTG aquifers, and overburden formations, can serve to permanently store CO₂ in the subsurface (Bakhshian et al., 2023; Bump et al., 2023; Ni et al., 2024). This storage configuration has been termed "composite confining systems" and those authors highlight the potential for such systems in Miocene aquifers around the Gulf of Mexico. From initial work, it would appear that some Malay Basin aquifers could be considered similarly, though further work would be required to evaluate the stratigraphic distribution of sandstone intervals, caprock properties and effectiveness and dynamic behaviour of the CO₂ plume.

6.3. Study limitations

This study also sought to develop an improvement to traditional GCS screening workflows, notably accounting for highly variable thermophysical CO₂ properties. The concept of screening geological basins for GCS potential is well established. Early studies such as Bachu (2003) and Chadwick et al. (2008) outlined the key criteria for consideration, and these have largely remained unchanged as the topic has advanced and GCS adoption has evolved. The thermophysical properties of CO₂ at reservoir conditions are known to be a key parameter when screening basins, but given many of these studies focused on old, cold basins with limited overpressure, usually an upper 800 m depth cut-off, paired with a lower depth cut-off (accounting for the reduction of porosity) is sufficient. That said, there has been more recent literature focused on incorporating variable subsurface temperature and pressure conditions into screening workflows (Baur and Hiebert, 2024; Bump et al., 2024). This study builds on that by also incorporating thermophysical property calculations in the screening workflow, while also adding a further step in the screening workflow of defining optimal injection zones and using cluster analysis to identify connected regions well-suited to follow-up GCS studies.

This study also assesses the regional-scale suitability of saline

aquifers using relatively little subsurface data (depth of aquifer, geothermal gradient, trendlines of porosity and pressure with depth, high-level fault mapping). By this design, and by utilising Python scripts and common file types (ASCII and raster files), it is intended that this workflow can be readily adopted, utilised for other basins and further developed when new data and/or knowledge becomes available.

However, by adopting this approach, there are naturally some limitations to the study. Relationships of porosity and pressure with depth are generalised, in this case owing to the sparse well data used. This could be improved with further incorporation of geological facies to better constrain porosity distribution and depositional environment modelling to consider reservoir quality trends away from well control points. The distribution of overpressures is also likely to be more complex than that presented here, and as outlined in subSection 5.3, we adopt an approach whereby the maximum possible overpressure for each region is calculated. In reality, transition zones and various overpressure trends have been noted in different wells, thus the degree of overpressure in these instances will be overestimated.

We also treat faults exclusively as high-risk and features to be avoided when screening optimal zones. Further work would be required to better understand the relative risk posed by different fault types, by analysing their geometry or looking for evidence of methane leakage from seismic datasets. Quick fault leakage screening tools (Ramachandran et al., 2024) could aid in pragmatically assessing the risk posed by certain faults in the basin.

Finally, this workflow focuses purely on the porosity of the aquifer, the phase and density of CO₂ at initial conditions within it, and the distance to major fault zones. We do not consider the effectiveness of the appropriate caprocks, or the permeability (injectivity) of the aquifer (though this is likely to be partially correlated with porosity). Nor did we conduct any reservoir simulations to analyse the impact of pressure and fluid properties on storage capacity and efficiency, despite their well-documented significance (de Jonge-Anderson et al., 2024a). However, this study allows for specific areas to be targeted for such analyses in future.

6.4. Sensitivity analysis

The use of cut-off values in calculating optimal GCS zones is recognised as both an uncertain and sensitive step in this study. Regarding petrophysical properties, a choice to constrain optimal zones to areas of porosity greater than 10 % and permeabilities greater than 100 mD was

made. However, an argument could also be made that lower porosity and permeability aquifers are perfectly adequate for GCS and could even bring added benefits such as more confined lateral CO₂ plume propagation (Zapata et al., 2020). To investigate the impact of porosity cut-off on calculated storage capacity, several capacity calculations were made for two different aquifers, using parameters identical to those described above, with the exception of porosity cut-off, which was varied from 5 % to 25 % (Fig. 13a and c). For the shallow aquifer, Group E (Fig. 13a), selection of lower cut-offs did not impact the result as this aquifer did not contain porosity values in that range. However, for the deeper aquifer, Group J (Fig. 13c), the impact of cut-off is profound, with the capacity decreasing by half if the cut-off if a more stringent cut-off of 15 % is used. This points to the importance of accurately constraining appropriate porosity cut-off values moving forward, perhaps by developing aquifer-specific cut-offs, informed by numerical simulations and/or core measurements to better understand the dynamics of plume behaviour for a range of petrophysical characteristics.

This exercise was repeated for CO₂ density by varying this value from 100 to 700 kg/m³ (Fig. 13b and d). For the shallow aquifer, decreasing the density cut-off to 200 kg/m³ results in a ~ 1.5 times increase in total storage capacity. This can appear counterintuitive as for the same area, a smaller density should result in lower storage capacity. However, by relaxing the threshold imposed on CO₂ density, a larger area of the basin is considered optimal, the effect of which appears to override the reduction in density. In this case, the capacity values should be treated with caution as they represent basin-scale, but impractical storage, when on the local-scale, CO₂ density is much lower than would be considered adequate for a GCS site.

7. Summary and conclusions

This study focused on assessing the suitability of saline aquifers in the Malay Basin for GCS using a screening workflow incorporating thermophysical properties and mapping of optimal injection zones. It also incorporated new analysis of subsurface datasets including depth structure maps based on hundreds of stratigraphic well tops, formation pressures from pressure-time measurements and analyses of depth, porosity and permeability relationships.

Of the eight aquifers evaluated in this work, seven contain optimal zones for GCS, though the spatial distribution of these varies by stratigraphic interval. The youngest, Pliocene-age aquifer is too shallow to store substantial amounts of CO₂, but upper Miocene intervals contain

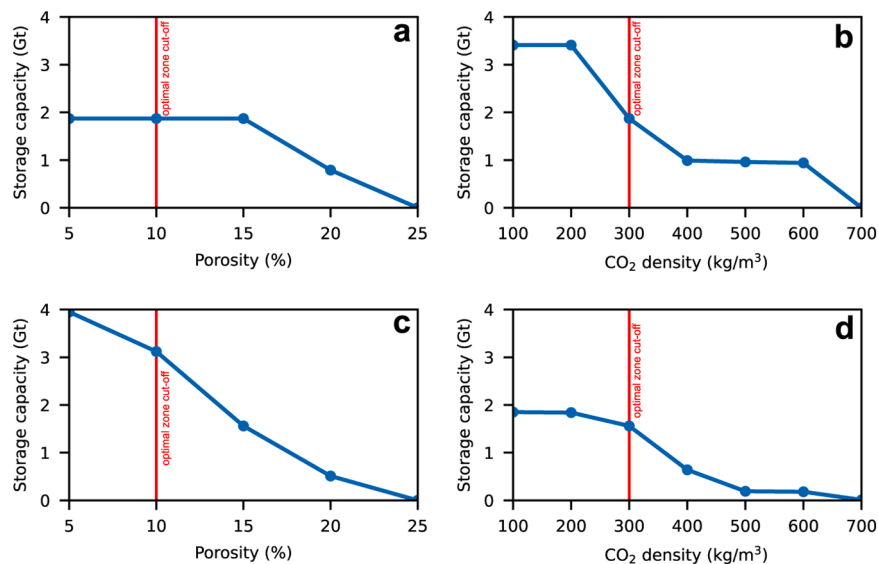


Fig. 13. Multi-panel plot illustrating the impact of different porosity (a, c) and CO₂ density (b, d) cut-offs on storage capacity. Examples for a shallow aquifer (Group E: a, b) and deep aquifer (Group J: c, d) are shown.

optimal zones in the northwest of the basin. These zones are located near high-CO₂ gas accumulations awaiting development. Middle Miocene intervals are too deep in the northwest of the basin but could be developed elsewhere as stacked GCS systems, given their low NTG. Oligocene-lower Miocene aquifers contain thicker sandstones, but their potential is constrained to the margins of the basin. The largest storage capacity modelled was within the thick, but low NTG Group I.

Overall, this study provides an important first step in the regional screening of saline aquifers in the Malay Basin and a framework for which to target detailed feasibility studies (e.g. within optimal zones adjacent to known CO₂ sources). Further work should seek to refine the uncertainties around some parameters (e.g., porosity) and/or determine more bespoke cut-offs for optimal zone identification based on laboratory or modelling studies.

CRedit authorship contribution statement

Iain de Jonge-Anderson: Writing – review & editing, Writing – original draft, Visualization, Methodology, Formal analysis, Conceptualization. **Hariharan Ramachandran:** Writing – review & editing, Formal analysis. **Ana Widyanita:** Writing – review & editing, Resources, Conceptualization. **Andreas Busch:** Writing – review & editing, Supervision. **Florian Doster:** Writing – review & editing, Supervision. **Uisdean Nicholson:** Writing – review & editing, Supervision, Conceptualization.

Declaration of competing interest

The authors declare that they have no known competing financial interests or personal relationships that could have appeared to influence the work reported in this paper.

Acknowledgements

The funding and data underpinning this work was provided by PETRONAS via the PETRONAS Centre of Excellence in Subsurface Engineering and Energy Transition (PACESET), based at Heriot-Watt University. SLB is thanked for providing academic licences for Petrel and Techlog. Petrosys are thanked for providing academic licences for Petrosys PRO and ESRI are thanked for providing academic licences for ArcGIS Pro, all of which facilitated this work.

Data availability

The data is available at this link: <https://doi.org/10.5281/zenodo.14761426>.

References

- Armitage, J.H., Viotti, C., 1977. Stratigraphic nomenclature-southern end Malay basin. Proc. Indon Petrol. Assoc., 6th Ann. Conv. Sixth Annual Convent. <https://doi.org/10.29118/IPA.1281.69.94>.
- Bachu, S., 2003. Screening and ranking of sedimentary basins for sequestration of CO₂ in geological media in response to climate change. Environ. Geol. 44 (3), 277–289. <https://doi.org/10.1007/s00254-003-0762-9>.
- Bachu, S., 2015. Review of CO₂ storage efficiency in deep saline aquifers. Int. J. Greenh. Gas Control 40, 188–202. <https://doi.org/10.1016/j.ijggc.2015.01.007>.
- Bakhshian, S., Bump, A.P., Pandey, S., Ni, H., Hovorka, S.D., 2023. Assessing the potential of composite confining systems for secure and long-term CO₂ retention in geosequestration. Sci. Rep. 13 (1), 21022. <https://doi.org/10.1038/s41598-023-47481-2>.
- Baur, F., Hiebert, S., 2024. Invasion percolation & basin modelling for CCS site screening and characterization. Greenh. Gas.: Sci. Technol. <https://doi.org/10.1002/ghg.2303>.
- Bell, I.H., Wronski, J., Quoilin, S., Lemort, V., 2014. Pure and pseudo-pure fluid thermophysical property evaluation and the open-source thermophysical property library CoolProp. Ind. Eng. Chem. Res. 53 (6), 2498–2508. <https://doi.org/10.1021/ie4033999>.
- Bump, A.P., Hovorka, S.D., Meckel, T.A., 2021. Common risk segment mapping: streamlining exploration for carbon storage sites, with application to coastal Texas

- and Louisiana. Int. J. Greenh. Gas Control 111, 103457. <https://doi.org/10.1016/j.ijggc.2021.103457>.
- Bump, A.P., Bakhshian, S., Ni, H., Hovorka, S.D., Olariu, M.I., Dunlap, D., Hosseini, S.A., Meckel, T.A., 2023. Composite confining systems: rethinking geologic seals for permanent CO₂ sequestration. Int. J. Greenh. Gas Control 126, 103908. <https://doi.org/10.1016/j.ijggc.2023.103908>.
- Bump, A.P., Hovorka, S.D., 2024. Pressure space: the key subsurface commodity for CCS. Int. J. Greenh. Gas Control 136, 104174. <https://doi.org/10.1016/j.ijggc.2024.104174>.
- Callas, C., Davis, J.S., Saltzer, S.D., Hashemi, S.S., Wen, G., Gold, P.O., Zoback, M.D., Benson, S.M., Kovscek, A.R., 2024. Criteria and workflow for selecting saline formations for carbon storage. Int. J. Greenh. Gas Control 135, 104138. <https://doi.org/10.1016/j.ijggc.2024.104138>.
- Chadwick, A., Arts, R., Bernstone, C., May, F., Thibeau, S., Zweigel, P., 2008. Best practice for the storage of CO₂ in saline aquifers—observations and guidelines from the SACS and CO2STORE projects (Vol. 14). Brit. Geol. Surv.
- Chadwick, R.A., Zweigel, P., Gregersen, U., Kirby, G.A., Holloway, S., Johannessen, P.N., 2004. Geological reservoir characterization of a CO₂ storage site: the Utsira Sand, Sleipner, Northern North Sea. Energy 29 (9–10), 1371–1381. <https://doi.org/10.1016/j.energy.2004.03.071>.
- Cheng, Y., Liu, W., Xu, T., Zhang, Y., Zhang, X., Xing, Y., Feng, B., Xia, Y., 2023. Seismicity induced by geological CO₂ storage: a review. Earth-Sci. Rev. 239, 104369. <https://doi.org/10.1016/j.earscirev.2023.104369>.
- de Jonge-Anderson, I., Ramachandran, H., Nicholson, U., Geiger, S., Widyanita, A., Doster, F., 2024a. Determining CO₂ storage efficiency within a saline aquifer using reduced complexity models. Adv. Geo-Energy Res. 13 (1), 22–31. <https://doi.org/10.46690/ager.2024.07.04>.
- de Jonge-Anderson, I., Widyanita, A., Busch, A., Doster, F., Nicholson, U., 2024b. New insights into the structural and stratigraphic evolution of the Malay Basin using 3D seismic data: implications for regional carbon capture and storage potential. Basin Res. 36 (4), e12885. <https://doi.org/10.1111/br.12885>.
- de Jonge-Anderson, I., Ramachandran, H., Widyanita, A., Busch, A., Doster, F., Nicholson, U., 2025. iaindejongeanderson/MalayBasin_CO2_Storage: Supplementary data for article “Regional screening of saline aquifers in the Malay Basin for CO₂ storage”. <https://doi.org/10.5281/zenodo.14761426>.
- Gasda, S.E., Nordbotten, J.M., Celia, M.A., 2009. Vertical equilibrium with sub-scale analytical methods for geological CO₂ sequestration. Comput. Geosci. 13 (4), 469–481. <https://doi.org/10.1007/s10596-009-9138-x>.
- GEBCO Bathymetric Compilation Group 2023. (2023). The GEBCO_2023 Grid—A continuous terrain model of the global oceans and land. (Version 1) [Documents, Network Common Data Form]. NERC EDS British Oceanographic Data Centre NOC. <https://doi.org/10.5285/F98B053B-0CBC-6C23-E053-6C86ABC0AF7B>.
- Gibson-Poole, C.M., Taplin, M., Bouffin, N., Duffy, L., Sutherland, F., Cabral, A., Ashby, D., 2024. Site characterization of the Endurance CO₂ Store, Southern North Sea, UK. Geoenery. <https://doi.org/10.1144/geoenergy2024-012>.
- Goodman, A., Hakala, A., Bromhal, G., Deel, D., Rodosta, T., Frailey, S., Small, M., Allen, D., Romanov, V., Fazio, J., Huerta, N., McIntyre, D., Kutchko, B., Guthrie, G., 2011. U.S. DOE methodology for the development of geologic storage potential for carbon dioxide at the national and regional scale. Int. J. Greenh. Gas Control 5 (4), 952–965. <https://doi.org/10.1016/j.ijggc.2011.03.010>.
- Gunter, W.D., Wong, S., Cheel, D.B., Sjoström, G., 1998. Large CO₂ sinks: their role in the mitigation of greenhouse gases from an international, national (Canadian) and provincial (Alberta) perspective. Appl. Energy 61 (4), 209–227. [https://doi.org/10.1016/S0306-2619\(98\)00042-7](https://doi.org/10.1016/S0306-2619(98)00042-7).
- Hasbollah, D.Z.A., Junin, R., Taib, A.M., & Mazlan, A.N. (2020). Basin evaluation of CO₂ geological storage potential in Malay Basin, Malaysia. In P. Duc Long & N. T. Dung (Eds.), Geotechnics For Sustainable Infrastructure Development (Vol. 62, pp. 1405–1410). Springer Singapore. https://doi.org/10.1007/978-981-15-2184-3_184.
- Hosseini, S.A., Ershadnia, R., Lun, L., Morgan, S., Bennett, M., Skrivanos, C., Li, B., Soltanian, M.R., Pawar, R., Hovorka, S.D., 2024. Dynamic modeling of geological carbon storage in aquifers – workflows and practices. Int. J. Greenh. Gas Control 138, 104235. <https://doi.org/10.1016/j.ijggc.2024.104235>.
- Hughes, D.S., 2009. Carbon storage in depleted gas fields: key challenges. Energy Proced. 1 (1), 3007–3014. <https://doi.org/10.1016/j.egypro.2009.02.078>.
- IEA, 2024. Asia Pacific Emissions. <https://www.iea.org/regions/asia-pacific/emissions> (accessed September 2024).
- IPCC, 2022. In: Mitigation of Climate Change Climate Change 2022 Working Group III Contribution to the Sixth Assessment Report of the Intergovernmental Panel on Climate Change.
- Jin, M., Mackay, E., Mathias, S., Pickup, G., 2014. Impact of sub seismic heterogeneity on CO₂ injectivity. Energy Proced. 63, 3078–3088. <https://doi.org/10.1016/j.egypro.2014.11.331>.
- Karolyte, R., Johnson, G., Yielding, G., Gilfillan, S.M.V., 2020. Fault seal modelling – the influence of fluid properties on fault sealing capacity in hydrocarbon and CO₂ systems. Petrol. Geosci. 26 (3), 481–497. <https://doi.org/10.1144/petgeo2019-126>.
- Krevor, S., de Coninck, H., Gasda, S.E., Ghaleigh, N.S., de Gooyert, V., Hajibeygi, H., Juanes, R., Neufeld, J., Roberts, J.J., Swennenhuis, F., 2023. Subsurface carbon dioxide and hydrogen storage for a sustainable energy future. Nat. Rev. Earth Environ. 4 (2), 102–118. <https://doi.org/10.1038/s43017-022-00376-8>.
- Lunt, P., 2021. A reappraisal of the cenozoic stratigraphy of the Malay and West Natuna Basins. J. Asia. Earth Sci.: X 5, 100044. <https://doi.org/10.1016/j.jaex.2020.100044>.
- Lynch, T., Fisher, Q., Angus, D., Lorinczi, P., 2013. Investigating stress path hysteresis in a CO₂ injection scenario using coupled geomechanical-fluid flow modelling. Energy Proced. 37, 3833–3841. <https://doi.org/10.1016/j.egypro.2013.06.280>.

- Madon, M.B. (1994). Depositional and diagenetic histories of reservoir sandstones in the Jerneh Field, central Malay Basin. <https://archives.datapages.com/data/geological-society-of-malaysia/bulletins/036/036001/pdfs/31.htm>.
- Madon, M., 2007. Overpressure development in rift basins: an example from the Malay Basin, offshore Peninsular Malaysia. *Petrol. Geosci.* 13 (2), 169–180. <https://doi.org/10.1144/1354-079307-744>.
- Madon, M., 2021. Five decades of petroleum exploration and discovery in the Malay Basin (1968–2018) and remaining potential. *Bull. Geol. Soc. Malay.* 72, 63–88. <https://doi.org/10.7186/bgsm72202106>.
- Madon, M., Yang, J.-S., Abolins, P., Abu Hassan, R., M. Yazkan, A., Zainal, S.B., 2006. Petroleum systems of the northern Malay Basin. *Bull. Geol. Soc. Malay.* 49, 125–134. <https://doi.org/10.7186/bgsm49200620>.
- Madon, M., Watts, 1998. Gravity anomalies, subsidence history and the tectonic evolution of the Malay and Penyu Basins (offshore Peninsular Malaysia). *Basin Res.* 10 (4), 375–392. <https://doi.org/10.1046/j.1365-2117.1998.00074.x>.
- Madon, M., Abolins, P., Hoesni, M.J., Ahmad, B., 1999. 'Malay Basin'. *The petroleum Geology and Resources of Malaysia*, Petronas, pp. 173–217. Kuala Lumpur.
- Madon, M., Jong, J., Kessler, F.L., Murphy, C., Your, L., A Hamid, M., M Sharef, N., 2019. Overview of the structural framework and hydrocarbon plays in the Penyu Basin, offshore Peninsular Malaysia. *Bull. Geol. Soc. Malay.* 68, 1–23. <https://doi.org/10.7186/bgsm68201901>.
- Madon, M., Jong, J., 2021. Geothermal gradient and heat flow maps of offshore Malaysia: some updates and observations. *Bull. Geol. Soc. Malay.* 71, 159–183. <https://doi.org/10.7186/bgsm71202114>.
- Mansor, M.Y., Rahman, A.H.A., Menier, D., Pubellier, M., 2014. Structural evolution of Malay Basin, its link to Sunda Block tectonics. *Mar. Pet. Geol.* 58, 736–748. <https://doi.org/10.1016/j.marpetgeo.2014.05.003>.
- Ministry of Economy (Malaysia), 2023. National Energy Transition Roadmap. https://www.ekonomi.gov.my/sites/default/files/2023-09/National/20Energy/20Transition/20Roadmap_0.pdf (accessed September 2024).
- Ni, H., Bump, A.P., Bakhshian, S., 2024. An experimental investigation on the CO₂ storage capacity of the composite confining system. *Int. J. Greenh. Gas Control* 134, 104125. <https://doi.org/10.1016/j.ijggc.2024.104125>.
- Ogland-Hand, J.D., Kammer, R.M., Bennett, J.A., Ellett, K.M., Middleton, R.S., 2022. Screening for geologic sequestration of CO₂: a comparison between SCO₂T^{PRO} and the FE/NETL CO₂ saline storage cost model. *Int. J. Greenh. Gas Control* 114, 103557. <https://doi.org/10.1016/j.ijggc.2021.103557>.
- Pedregosa, F., Varoquaux, G., Gramfort, A., Michel, V., Thirion, B., Grisel, O., Blondel, M., Prettenhofer, P., Weiss, R., Dubourg, V., Vanderplas, J., Passos, A., Cournapeau, D., Brucher, M., Perrot, M., Duchesnay, É., 2011. Scikit-learn: machine learning in python. *J. Mach. Learn. Res.* 12 (85), 2825–2830. <http://jmlr.org/papers/v12/pedregosa11a.html>.
- PETRONAS. (2022). Geological & geophysical information of the Malay Basin. Malaysia Bid round 2022. <https://www.petronas.com/sites/mpm/files/2022-07/M-BR-2022-Regional-Overview-Peninsular-Malaysia.pdf> (accessed June 2024).
- PETRONAS. (2024a). <https://www.petronas.com/mpm/media/media-releases/petronas-inks-2-dro-clusters-production-sharing-contracts-boost-gas-supply> (accessed September 2024).
- PETRONAS. (2024b). <https://www.petronas.com/media/media-releases/petronas-acquires-land-carbon-capture-and-storage-hub-peninsular-malaysia> (accessed September 2024).
- Proietti, G., Conti, A., Beaubien, S.E., Bigi, S., 2023. Screening, classification, capacity estimation and reservoir modelling of potential CO₂ geological storage sites in the NW Adriatic Sea, Italy. *Int. J. Greenh. Gas Control* 126, 103882. <https://doi.org/10.1016/j.ijggc.2023.103882>.
- Ramachandran, H., de Jonge-Anderson, I., Hafizi Musa, I., Nicholson, U., Tan, C.P., Geiger, S., Doster, F., 2024. Rapid Fault Leakage Modeling for CO₂ Storage in Saline Aquifers. <https://doi.org/10.31223/X5S12N>.
- Ramírez, A., Hagedoorn, S., Kramers, L., Wildenborg, T., Hendriks, C., 2010. Screening CO₂ storage options in The Netherlands. *Int. J. Greenh. Gas Control* 4 (2), 367–380. <https://doi.org/10.1016/j.ijggc.2009.10.015>.
- Ramli, M.N., 1988. Stratigraphy and palaeofacies development of Carigali's operating areas in the Malay Basin, South China Sea. *Bull. Geol. Soc. Malay.* 22, 153–187. <https://doi.org/10.7186/bgsm22198808>.
- Raza, A., Rezaee, R., Gholami, R., Bing, C.H., Nagarajan, R., Hamid, M.A., 2016. A screening criterion for selection of suitable CO₂ storage sites. *J. Nat. Gas Sci. Eng.* 28, 317–327. <https://doi.org/10.1016/j.jngse.2015.11.053>.
- Reuters. (2023). <https://www.reuters.com/sustainability/climate-energy/japan-petronas-discuss-storing-japanese-co2-malaysian-sites-2023-09-27/> (accessed September 2024).
- Rizzo, R.E., Inskip, N.F., Fazeli, H., Betlem, P., Bisdom, K., Kampman, N., Snippe, J., Senger, K., Doster, F., Busch, A., 2024. Modelling geological CO₂ leakage: integrating fracture permeability and fault zone outcrop analysis. *Int. J. Greenh. Gas Control* 133, 104105. <https://doi.org/10.1016/j.ijggc.2024.104105>.
- Rodosta, T.D., Litynski, J.T., Plasynski, S.I., Hickman, S., Frailey, S., Myer, L., 2011. U.S. Department of Energy's site screening, site selection, and initial characterization for storage of CO₂ in deep geological formations. *Energy Proced.* 4, 4664–4671. <https://doi.org/10.1016/j.egypro.2011.02.427>.
- Slater, J.G., Christie, P.A.F., 1980. Continental stretching: an explanation of the post-mid-cretaceous subsidence of the Central North Sea Basin. *J. Geophys. Res.: Solid Earth* 85 (B7), 3711–3739. <https://doi.org/10.1029/JB085iB07p03711>.
- Shariff, Bin, Kader, M., 1994. Abnormal pressure occurrence in the Malay and Penyu basins, offshore Peninsular Malaysia – a regional understanding. *Bull. Geol. Soc. Malay.* 36, 81–91.
- Snippe, J., Kampman, N., Bisdom, K., Tambach, T., March, R., Maier, C., Phillips, T., Inskip, N.F., Doster, F., Busch, A., 2022. Modelling of long-term along-fault flow of CO₂ from a natural reservoir. *Int. J. Greenh. Gas Control* 118, 103666. <https://doi.org/10.1016/j.ijggc.2022.103666>.
- Spencer, A.M., Larsen, V.B., 1990. Fault traps in the Northern North Sea. *Geol. Soc. 55* (1), 281–298. <https://doi.org/10.1144/gsl.sp.1990.055.01.13>.
- Storegga. (2024). <https://storegga.earth/news/storegga-joins-forces-with-global-leaders-to-evaluate-offshore-ccs-in-malaysia> (accessed September 2024).
- Straume, E.O., Gaina, C., Medvedev, S., Hochmuth, K., Gohl, K., Whittaker, J.M., Abdull Fattah, R., Doornbal, J.C., Hopper, J.R., 2019. Globseed: updated total sediment thickness in the world's oceans. *Geochim. Geophys. Geosyst.* 20 (4), 1756–1772. <https://doi.org/10.1029/2018GC008115>.
- Sun, X., Cao, Y., Liu, K., Alcalde, J., Cabello, P., Travé, A., Cruset, D., Gomez-Rivas, E., 2023. Effects of fluvial sedimentary heterogeneity on CO₂ geological storage: integrating storage capacity, injectivity, distribution and CO₂ phases. *J. Hydrol.* 617, 128936. <https://doi.org/10.1016/j.jhydrol.2022.128936>.
- Tingay, M.R.P., Morley, C.K., Laird, A., Limpompipat, O., Krisadasima, K., Pabchanda, S., Macintyre, H.R., 2013. Evidence for overpressure generation by kerogen-to-gas maturation in the northern Malay Basin. *Am. Assoc. Pet. Geol. Bull.* 97 (4), 639–672. <https://doi.org/10.1306/09041212032>.
- Tjia, H.D., Liew, K.K., 1996. Changes in tectonic stress field in northern Sunda Shelf basins. *Geol. Soc., Lond.* 106 (1), 291–306. <https://doi.org/10.1144/GSL.SP.1996.106.01.19>.
- TotalEnergies. (2023). <https://totalenergies.com/media/news/press-releases/totalenergies-partners-petronas-and-mitsui-carbon-storage-hub-malaysia> (accessed September 2024).
- van der Meer, L.G.H., 1995. The CO₂ storage efficiency of aquifers. *Energy Convers. Manage.* 36 (6–9), 513–518. [https://doi.org/10.1016/0196-8904\(95\)00056-J](https://doi.org/10.1016/0196-8904(95)00056-J).
- Wang, Y., Zhang, K., Wu, N., 2013. Numerical investigation of the storage efficiency factor for CO₂ geological sequestration in saline formations. *Energy Proced.* 37, 5267–5274. <https://doi.org/10.1016/j.egypro.2013.06.443>.
- Wendt, A., Sheriff, A., Shih, C.Y., Vikara, D., Grant, T., 2022. A multi-criteria CCUS screening evaluation of the Gulf of Mexico, USA. *Int. J. Greenh. Gas Control* 118, 103688. <https://doi.org/10.1016/j.ijggc.2022.103688>.
- Wibberley, C.A.J., Yielding, G., Di Toro, G., 2008. Recent advances in the understanding of fault zone internal structure: a review. *Geol. Soc., Lond.* 299 (1), 5–33. <https://doi.org/10.1144/sp299.2>.
- Wijaya, N., Morgan, D., Vikara, D., Grant, T., Liu, G., 2024. Basin-scale study of CO₂ storage in stacked sequence of geological formations. *Sci. Rep.* 14 (1), 18661. <https://doi.org/10.1038/s41598-024-66272-x>.
- Wu, L., Thorsen, R., Ottesen, S., Meneguolo, R., Hartvedt, K., Ringrose, P., Nazarian, B., 2021. Significance of fault seal in assessing CO₂ storage capacity and containment risks – an example from the Horda Platform, northern North Sea. *Petrol. Geosci.* 27 (3). <https://doi.org/10.1144/petgeo2020-102> petgeo2020-102.
- Yakzan, A., Harun, A., Md Nasib, B., Morley, R.J., 1996. Integrated biostratigraphic zonation for the Malay Basin. *Bull. Geol. Soc. Malay.* 39, 157–184. <https://doi.org/10.7186/bgsm39199615>.
- Zapata, Y., Kristensen, M.R., Huerta, N., Brown, C., Kabir, C.S., Reza, Z., 2020. CO₂ geological storage: critical insights on plume dynamics and storage efficiency during long-term injection and post-injection periods. *J. Nat. Gas Sci. Eng.* 83, 103542. <https://doi.org/10.1016/j.jngse.2020.103542>.
- Zhang, K., Lau, H.C., 2022. Regional opportunities for CO₂ capture and storage in Southeast Asia. *Int. J. Greenh. Gas Control* 116, 103628. <https://doi.org/10.1016/j.ijggc.2022.103628>.
- Zhang, Y., Jackson, C., Krevor, S., 2024. The feasibility of reaching gigatonne scale CO₂ storage by mid-century. *Nat. Commun.* 15 (1), 6913. <https://doi.org/10.1038/s41467-024-51226-8>.